CHAPTER 9

Subsidence and thermal history

Accuse not Nature, she hath done her part;
Do thou but thine.

(JOHN MILTON, *PARADISE LOST* (1667))

SUMMARY

The burial of sedimentary layers in a basin causes porosity loss, which may be due to mechanical compaction, physicochemical changes such as pressure solution, and cementation. Most procedures used in the study of subsidence in sedimentary basins assume that there is no change in the solid volume during burial, so that mechanical compaction of framework grains due to increasing compression from the overlying sediment-water column solely drives porosity reduction. Despite the fact that this is manifestly not true, quantitative incorporation of the effects of cementation and pressure solution are still in their infancy.

Present-day stratigraphic thicknesses are a product of cumulative changes in rock volume through time. A quantitative analysis of subsidence rates through time, sometimes called *geohistory analysis*, relies primarily on the decompaction of stratigraphic units to their correct thickness at the time of interest. Two other corrections must also be made in order to plot subsidence relative to a fixed datum such as present sea level. These are: (i) corrections for the variations in depositional water depth through time, and (ii) corrections for absolute fluctuations of sea level (eustasy) relative to the present sea-level datum.

The decompaction of stratigraphic units requires the variation of porosity with depth to be known. Some sedimentary formations exhibit a linear relation between porosity and depth but, self-evidently, a linear relationship cannot hold at large depths since porosities would become negative. Estimates of porosity from borehole logs (such as the sonic log) for a wide range of different lithologies suggest that normally pressured sediments exhibit an exponential relationship of the form $\phi = \phi_0 e^{-cy}$, where ϕ is the porosity at any depth y, ϕ_0 is the surface porosity, and c is a coefficient that is dependent on lithology and describes the rate at which the exponential decrease in porosity takes place with depth. There are a number of different formulations of this exponential relationship, with different pre-exponential factors and exponents. The driving force for compaction is the effective stress acting at grain–grain contacts. Since the total lithostatic stress is the sum of the effective stress and the pore fluid pressure, overpressuring of pore fluids trapped in a formation has the effect of inhibiting compaction. This causes strong deviations from the expected porosity–depth curve in the overpressured units. Overpressuring can be predicted from a dimensionless parameter representing the ratio of hydraulic conductivity to rate of sediment accumulation.

Information on changing paleobathymetry through time may come from sedimentary facies and distinctive geochemical signatures, but principally from micropaleontological studies. Benthic microfossils are especially useful. Eustatic corrections are hazardous to apply and a simple transferral from the Vail–Haq curve is not recommended. Correction for the widely accepted long-term eustatic variation of sea level is, however, justified.

The sediment deposited in a marine basin replaces water, and so drives further subsidence of the basement. The exercise of partitioning the subsidence due to tectonics and that due to sediment loading is termed *backstripping*. If the lithosphere is in local Airy isostasy, the decompacted subsidence, corrected for paleobathymetric and eustatic variations, can be simply used to calculate

the tectonic component. This requires the average bulk density of the sediment column as a function of time to be calculated. However, if the lithosphere supports the sediment load by a regional flexure, the separation of the tectonic and sediment contributions is more complex. The flexural loading of the sedimentary basin can be accounted for if both the flexural rigidity and spatial distribution of the sediment load are known.

Subsidence in sedimentary basins causes thermal maturation in the progressively buried sedimentary layers. Indicators of the thermal history include organic, geochemical, mineralogical, and thermochronometric parameters. The most important factors in the maturation of organic matter are temperature and time, pressure being relatively unimportant. This temperature and time dependency is described by the *Arrhenius equation*, which states that the reaction rate increases exponentially with temperature; the rate of the increase, however, slows with increasing temperature because the materials undergoing thermal maturation are used up. The cumulative effect of increasing temperature over time can be evaluated by integrating the reaction rate over time. This is called the *maturation integral*. It can be related directly to measurable indices of burial.

Paleotemperatures are controlled by the basal heat flow history of the basin (which in turn reflects the lithospheric mechanics), but also by internal factors such as variations in thermal conductivities, heat generation from radioactive sources in the continental crust and within the sedimentary basin-fill, regional water flow through aquifers, and surface temperature variation. Thermal conductivity models of the basin-fill can be developed from knowledge of framework mineralogy and porosity. The effect of a heterogeneous basin-fill, assuming a constant heat flow, is an irregular rather than linear geotherm. Radiogenic heat production is greatest where the underlying basement is granitic, and where the basin-fill contains "hot" shales. Radiogenic heat production is particularly important in deep, long-lived basins. Advection of fluids has profound consequences for heat flow in basins and can locally override basal heat flow contributions. Advective heat transport depends on the temperature of the pore fluids but also on rock porosity. Although compactionally driven fluid movement is slow and thermally relatively ineffective, gravitationally driven flow through aquifers is very important. Recharge areas of water in topographically elevated areas around the basin margin, such as in foreland basins and intracratonic sags, displaces basinal brines and strongly affects the temperature history of basin sediments. Major climatic changes of long frequency cause temperature changes to be propagated through the upper part of the basin-fill that may affect thermal indicators.

Formation temperatures can be estimated from borehole measurements, with a correction applied to account for the cooling that takes place during the circulation of drilling fluids. These corrected formation temperatures allow geothermal gradients to be calculated.

Vitrinite reflectance is the most widely used organic indicator of thermal maturity. Other organic and mineralogical indicators are also used. Apatite fission track analysis is now a well-established thermochronological tool, but the diffusion of helium during U–Th decay is a promising emerging technique. Both thermochronometers allow the timing of thermal events as well as the maximum paleotemperature to be assessed.

Vitrinite reflectance measurements plotted against depth – termed R_o profiles – provide useful information on the thermal history of the basin. The "normal" pattern is a sublinear relationship between log R_o and depth, indicating a continuous, time-invariant geothermal gradient. R_o profiles with distinct kinks between two linear segments (doglegs) indicate two periods of different geothermal gradient separated by a thermal event. R_o profiles with a sharp break or jump (offsets) indicate the existence of an unconformity with a large stratigraphic gap. The R_o profile in basins that have undergone continuous subsidence intersect the surface at values of 0.2–0.4% R_o. Inverted basins that have lost the upper part of the basin-fill by crustal uplift and erosion have profiles intersecting the surface at higher values of R_o. The offset of the R_o profile from the "normal" profile can be used to estimate the amount of denudation, but care needs to be taken with the possible effects of thermal conductivity variations in the basin and the correct choice of surface temperature at the time of maximum paleotemperature of the basin-fill.

Studies of present-day heat flows and ancient geothermal gradients suggest that thermal regime closely reflects tectonic history. In particular, *hypothermal* (cooler than average) basins include ocean trenches and outer forearcs and foreland basins. *Hyperthermal* (hotter than average) basins include oceanic and continental rifts, some strike–slip basins with mantle involvement, and magmatic arcs in collisional settings. Mature passive margins that are old compared with the thermal time constant of the lithosphere tend to have near-average heat flows and geothermal gradients.

9.1 INTRODUCTION TO GEOHISTORY ANALYSIS

Improvements in the dating of stratigraphic units and in estimates of paleobathymetry, largely brought about by advances in micropaleontology, have allowed the development of quantitative techniques in geological analysis of sedimentary basins. Van Hinte (1978) termed this quantitative approach *geohistory analysis*. The first qualitative attempts at plotting subsidence/uplift and paleowater depth as a function of time date back at least to Lemoine's *Géologie du Bassin de Paris* published in 1911. Quantitative geohistory analysis was developed in the 1970s, principally in response to a vastly improved commercial paleontological data base.

Geohistory analysis aims at producing a curve for the subsidence and sediment accumulation rates through time. In order to do this, three corrections to the present stratigraphic thicknesses need to be carried out:

- *Decompaction*: present-day stratigraphic thicknesses must be corrected to account for the progressive loss of porosity with depth of burial;
- *paleobathymetry*: the water depth at the time of deposition determines its position relative to a datum (such as present-day sea level);
- *absolute sea level fluctuations*: changes in the paleosea level relative to today's also needs to be considered (see §8.3.4).

Having made these corrections, comparisons between boreholes or other sections are readily made possible. In addition, the subsidence curves give an immediate visual impression of the nature of the driving force responsible for basin formation and development (§9.3.5).

The time–depth history of any sediment layer can be evaluated therefore if the three corrections above can be applied. Such a time-depth history can also be tested from independent methods. These fall into the main classes of organic thermal indicators (§9.7.2), thermochronometric indicators (§9.7.3–9.7.4) and mineralogical thermal indicators (§9.7.5).

The addition of a sediment load to a sedimentary basin causes additional subsidence of the basement. This is a simple consequence of the replacement of water ($\rho = 1000\,\mathrm{kg\,m^{-3}}$), or less commonly air, by sediment ($\rho \sim 2500\,\mathrm{kg\,m^{-3}}$). The total subsidence is therefore partitioned into that caused by the tectonic driving force and that due to the sediment load. The way in which this partitioning operates depends on the isostatic response of the lithosphere (§2.3.2–§2.3.3). The simplest assumption is that any vertical column of load is compensated locally (Airy isostasy). This implies that the lithosphere has no strength to support the load. Alternatively, the lithosphere may transmit stresses and deformations laterally by a regional flexure. The same load will therefore cause a smaller subsidence in the case of a lithosphere with a strength sufficient to cause flexure. The technique whereby the effects of the sediment load are removed from the total subsidence to obtain the tectonic contribution is called *backstripping*. Backstripped subsidence curves are useful in investigating the basin-forming mechanisms (§9.3.5).

Burial history and thermal history can be used to determine the oil and gas potential of a basin and to estimate reservoir porosities. Burial history curves from a number of locations can also be used to construct paleostructure maps at specific time slices. Combined with information on thermal maturity, this can be a powerful tool in evaluating the timing of oil migration and likely migration pathways in relation to the development of suitable traps (see Chapter 10 for fuller discussion).

9.2 POROSITY LOSS DURING BASIN SUBSIDENCE

9.2.1 Porosity loss: mechanical compaction, physicochemical compaction, and cementation

Progressive burial of sediment by overlying layers during basin evolution causes a number of physical and chemical changes to the basin-fill. In this chapter we are primarily concerned with the loss of porosity, increase in bulk density and decrease in stratigraphic thickness that accompany burial, and in the changes resulting from thermal maturation. The implications of basin subsidence for petroleum systems, particularly the generation of petroleum fluids and reservoir quality, are dealt with in Chapter 10.

It is initially important to define some terminology. *Compaction* is the change in dimensions of a volume of sediment as a result of loading, which commonly takes the form of the gravitational load of an overlying column of water-saturated sediment. Compaction is therefore a strain. *Porosity loss* refers to the loss of pore volume that commonly accompanies burial, and may or may not be related to volumetric strains. For example, cementation of a sandstone may result in a loss of porosity but may not affect the volume occupied by the sedimentary rock,

and therefore involves no strain. Compaction and porosity loss are affected by three sets of interrelated processes (Giles 1997):

1 Mechanical compaction, which is the mechanical rearrangement and compression of grains in response to loading;
2 physicochemical compaction due to processes such as pressure solution, which is particularly important in carbonates;
3 cementation, which involves the filling of pore space by chemical precipitation, which is related to temperature rather than to loading.

For a given lithology, observations show that there is a general exponential porosity reduction and increase in bulk density with depth. The following sections therefore aim to explain this trend and to highlight important consequences for basin analysis.

The total volume of a sedimentary rock is made of a solid volume V_s and pore volume V_f. During burial the total volumetric strain is therefore made of a change in pore volume and a change in volume of the solid phase. Compaction causes a major reduction in the pore fluid volume accompanied by a small reduction of the solid volume due to compression, whereas cementation increases the solid volume at the expense of the pore fluid volume. Changes in the solid volume during mineral transformation and cementation are commonplace. For example, the transformation of aragonite to calcite causes an increase in 8% by volume, but the dehydration of gypsum to anhydrite causes a reduction of 37.5% in volume, and dehydration reactions in shales such as the illitization of K-feldspar and kaolinite causes a volume decrease of 9.6%. This means that the common starting point to the study of the loss of porosity during burial, the assumption that the solid volume remains constant (since the compressibilities of many rock-forming minerals are small) (Schneider et al. 1993) is prone to error.

9.2.2 The idea of effective stress

General relationships for the burial of sedimentary layers can be obtained using basic principles of soil mechanics. For a water-saturated clay for example, the overlying weight on a layer of sediment is supported jointly by the fluid pressure in the pores and the grain to grain mechanical strength of the clay aggregates:

$$\text{Effective stress } \sigma = \text{vertical compressive stress s} - \text{fluid pressure } p \tag{9.1}$$

This well-known relationship is known as *Terzaghi's law* (Terzaghi 1936; Terzaghi and Peck 1948). As the amount of gravitational compaction increases, the effective stress also increases. Since the vertical compressive stress s is determined by the weight of the overlying water-saturated sediment column,

$$s = \bar{\rho}_b g y \tag{9.2}$$

(where $\bar{\rho}_b$ is average water-saturated bulk density, g is acceleration due to gravity, and y is depth), this increasing vertical load must be divided between p and σ.

If the ratio of fluid pressure to overburden pressure $p/s = \lambda$, it must vary between zero where the fluid pressure is nonexistent, to 1 where the sediment layer is effectively "floating" on the highly pressured pore-filling fluid. We can therefore write

$$p = \lambda s = \lambda \bar{\rho}_b g y \tag{9.3}$$

and

$$\sigma = (1 - \lambda)\bar{\rho}_b g y \tag{9.4}$$

As the sediment load is increased, the extra vertical stress is taken up initially by an increase in pore fluid pressure so that both p and λ increase. With time, however, water is expelled from the pores, reducing fluid pressures but increasing effective stresses. The increase in σ results in compaction of the grains supporting the stresses, reducing porosity. The lowest pressure that the pore fluid can attain is that due to the hydrostatic column, that is

$$p = \rho_w g y \tag{9.5}$$

in which case

$$\lambda = \frac{\rho_w}{\bar{\rho}_b} \tag{9.6}$$

This is called the normal pressure since the pore fluids are at a pressure equivalent to the head of a static body of water and the grain–grain contacts are supporting the formation. If $\lambda > \rho_w/\bar{\rho}_b$, the pore fluids are at a higher pressure than hydrostatic.

Assuming that water is free to be expelled from the sediment pore space and is not trapped, increasing burial

should lead to the equilibrium state where p is hydrostatic. If this is the case, from (9.4) and (9.6)

$$\sigma = (\bar{\rho}_b - \rho_w)gy \tag{9.7}$$

which states that the magnitude of the stress causing compaction is a function of depth and the difference between the water-saturated sediment and water densities.

It is commonly assumed that the effective stress is a function of the porosity. Drawing on soil mechanics literature (Burland 1990), Audet and McConnell (1992) related the effective stress to a void ratio e equal to $\phi/(1-\phi)$ where ϕ is the porosity:

$$\sigma = \sigma_1 \exp\left(\frac{e_1 - e}{C/\ln(10)}\right) \tag{9.8}$$

where σ_1 is an effective stress at some reference void ratio e_1, and C is a constant known as the *compression index* reflecting sediment strength. Both σ_1 and C can be determined from compression tests and are typically 1.62 and 0.5 MPa respectively.

The Terzhagi law is a statement of the importance of fluid pressures, but it is not an explanation of the physical processes leading to normally pressured and overpressured sediments. Audet and McConnell (1992, 1994) proposed a dimensionless sedimentation parameter α given by

$$\alpha = \frac{\kappa_1}{V_0}\left(\frac{\rho_s}{\rho_f} - 1\right) \tag{9.9}$$

where κ_1 is the hydraulic conductivity of the sediments (typical values of 10^{-7} to 10^{-9} mm s^{-1}, Olsen 1960), which is dependent on permeability, fluid viscosity, and density as well as clay mineralogy, V_0 is the time-averaged sedimentation rate (typical values of 0.1 to 1 mm yr^{-1}), and ρ_s and ρ_f are the sediment and pore fluid densities respectively (typically 2700 and 1050 kg m^{-3}). The sedimentation parameter is the ratio of the rate at which pore fluid moves through the sediments *versus* the rate at which new sediment accumulates as an overburden at the depositional surface. Consequently, if $\alpha >> 1$, fluid is expelled from the compacting sediment relatively fast, leading to normally pressured pore fluids. In contrast, if $\alpha << 1$, pore fluid is retained in the compacting sediment, probably caused by fast sediment accumulation rates, leading to overpressured pore fluid.

9.2.3 Measuring porosity in the subsurface

As a prerequisite for a discussion of compaction and porosity loss during burial, it is important to have some understanding of how porosity can be estimated in the subsurface. Porosity can be directly measured on core and sidewall cores recovered from a borehole, but such direct measurements tend to be concentrated on zones of known economic interest, such as reservoir intervals (see below, Fig. 9.1a). The distribution of porosity with depth in a borehole must therefore be obtained by remote methods, principally from the interpretation of downhole electrical logs. For example, sonic, neutron, and density logs are sensitive to formation lithology and porosity.

The *sonic log* is a recording of the time taken (interval transit time, Δ_t) for a compressional sound wave emitted from a sonic sonde to travel across 1 foot (*c.* 25 cm) of formation to a receiver. The interval transit time is the inverse of velocity, which is a function of lithology and porosity. When lithology is known from other data such as a drill cuttings log, Δ_t may be used to calculate porosity from the *Wyllie time-average equation*:

$$\Delta_t = \Delta_{t\,ma}(1-\phi) + \phi(\Delta_{t\,f}) \tag{9.10}$$

where $\Delta_{t\,ma}$ is the transit time through the solid rock matrix (51.3–55.5 μs ft^{-1} for sandstones, 43.5–47.6 μs ft^{-1} for limestones), and $\Delta_{t\,f}$ is the transit time through the pore space fluid (dependent on fluid salinity, 189 μs ft^{-1} for fresh water). Rearranging equation (9.10), a solution is obtained for porosity:

$$\phi = \frac{\Delta_t - \Delta_{t\,ma}}{\Delta_t - \Delta_{t\,f}} \tag{9.11}$$

Instead of using equation (9.11) for each porosity determination, it may be more convenient to use a chart such as those provided by Schlumberger (1974). It has been found that in uncompacted, geologically young sands, the Wyllie time-average equation needs to be corrected by a compaction factor.

The principle of the *density log* is that gamma rays are emitted by a radioactive source in the logging tool, and are scattered and lose energy as a result of collisions with electrons in the formation. The number of scattered gamma rays recorded at a detector, also on the logging tool, depends on the density of electrons in the forma-

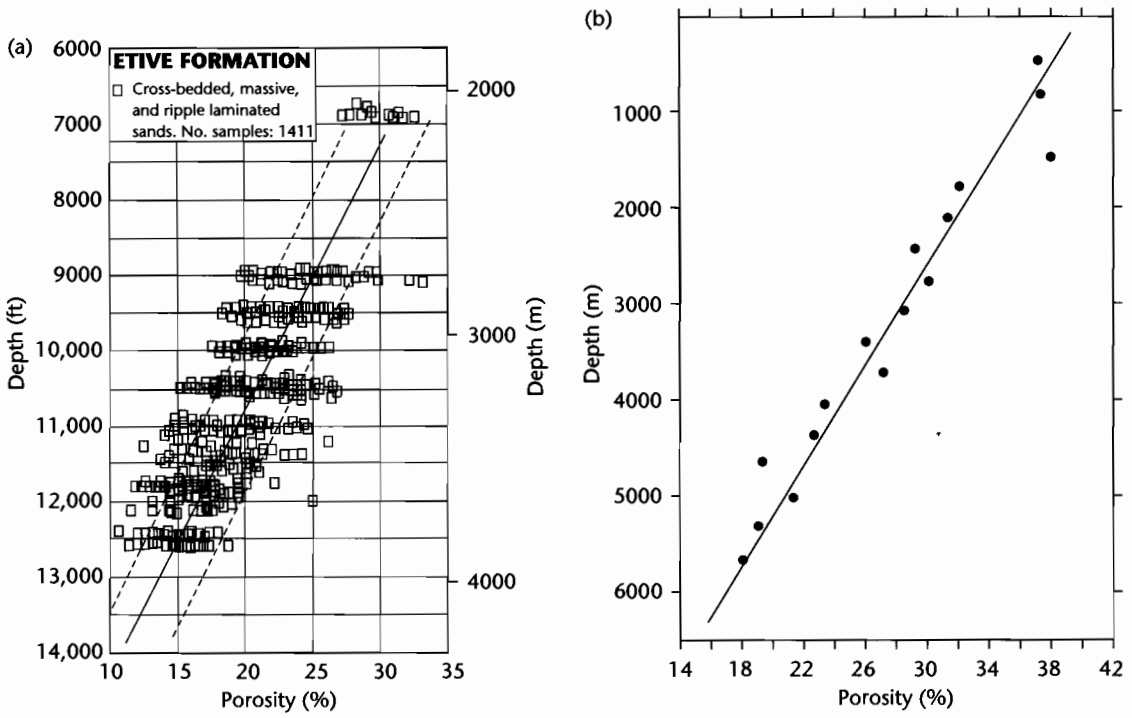

Fig. 9.1 Examples of a linear relationship between porosity and depth. (a) Cross-bedded, massive, and ripple-laminated sandstones from the Jurassic Etive Formation, Brent Group of the North Sea, from Giles (1997). Dashed lines give the 90% confidence interval for porosity about the regression line. Plot is based on 1411 samples; (b) Tertiary sands, southern Louisiana, based on over 17,000 cores, averaged every 1000 ft (*c.* 300 m), after Blatt (1979). The reduction in sand porosity with depth is thought to be due to the compaction of ductile rock fragments. Reproduced courtesy of Springer.

tion. This electron density is virtually the same as the formation bulk density for most common minerals, although for some evaporite minerals such as rock salt and sylvite (KCl), and coal, there is a significant difference.

The *Formation Density* (FDC) sonde is normally calibrated in fresh-water filled limestone formations, so that the log reads the actual bulk density for limestone and for fresh water. The bulk density ρ_b is a function of the average density of the substances making up the formation, that is, both the rock matrix and fluid-filled pores, and the relative volumes occupied, as shown by the equation

$$\rho_b = \phi\rho_f + (1-\phi)\rho_{ma} \tag{9.12}$$

where ρ_f is the average density of the fluid occupying the pore space, which is a function of temperature, pressure and salinity, and ρ_{ma} is the average density of the rock matrix. By rearranging equation (9.12) we very easily arrive at a means to determine porosity:

$$\phi = \frac{\rho_{ma} - \rho_b}{\rho_{ma} - \rho_f} \tag{9.13}$$

ρ_{ma} may itself be decomposed into its constituent parts. When clay minerals are present, a correction that accounts for the density and amount of clay may be needed in order to avoid inaccurate porosity determination,

$$\rho_b = \phi\rho_f + V_{clay}\cdot\rho_{clay} + (1-\phi-V_{clay})\rho_{ma} \tag{9.14}$$

where ρ_{clay} is the average density of the clay and V_{clay} is the fraction of the total rock occupied by clay. The clay correction is substantial when ρ_{ma} and ρ_{clay} are very dif-

ferent. This is usually at shallow depths where the clay is particularly uncompacted. Hydrocarbons may also lower the density log recording. Generally, the presence of oil in the invaded zone pore space has a negligible effect on the density log, but residual gas has a considerable effect that must be corrected for.

The principle of the *neutron log* is that neutrons emitted from a radioactive source collide with formation nuclei and are captured. A detector, or detectors, counts the returning neutrons. Because neutrons lose most energy when they collide with a hydrogen nucleus in the formation, the neutron log gives a measure of the hydrogen content, that is, the liquid-filled content of the formation. It can be used, therefore, to determine porosity. The most commonly used neutron tool is the *Compensated Neutron Log* (CNL). The CNL is calibrated to read true porosity in clean limestone formations. Its unit of measurement, as presented on the log, is therefore the "limestone porosity unit." When measuring in lithologies other than limestone, for example in a quartzose sandstone, a correction needs to be made.

The neutron log responds to *all* the hydrogen present in the formation, including the water bound up in clay minerals. As a result, it is very sensitive to clay content. In shales, the neutron log normally shows a very high reading, and needs correction. Although oil has a hydrogen content close to water and has only a small effect on the CNL, the hydrogen content of gas is considerably lower. As a result, the neutron response is low in formations that contain gas within the depth of investigation of the tool (generally <30 cm).

Of all the porosity tools, the sonic log is most widely used (e.g., Magara 1976; Ware and Turner 2002). This is largely because the neutron and density logs are normally only run in the deeper zones of hydrocarbon interest in a borehole, and the sonic log may therefore be the only porosity log available in the shallow sections of the borehole. Porosity from the sonic log can be determined if the lithology is known. The most common method of obtaining porosity from the density and neutron logs is to cross-plot them. The techniques and corrections necessary are given in manuals such as Schlumberger (1974) or Rider (1996).

Precise porosity determinations can be made on samples of the formation penetrated by a borehole. During a logging run, small sidewall cores can be obtained by firing a sleeved bullet into the formation. Intervals of reservoirs that are cored provide more promising material for porosity and permeability determination. Samples are drilled out of the slabbed core and analysed in the laboratory. Porosity trends with depth can then be obtained from a particular geological province if the same reservoir is cored at a wide range of different depths.

9.2.4 Porosity–depth relationships

Observations on the porosity–depth relationship of sedimentary rocks come from rock deformation experiments and from measurements from natural subsurface settings.

Rock deformation tests show that compaction rate is a strong function of mineralogy, with a linear relationship between log porosity and effective stress. Clays compact easily and quartz-rich lithologies compact relatively slowly. There are important deviations from this behavior. For example, sandstones with ductile lithic clasts compact more quickly than the linear relationship between log porosity and effective stress.

Direct measurements on core material and remote measurements from downhole logging devices provide an enormous database on the relation between present depth and porosity (Fig. 9.1). A number of factors affect the porosity–depth relationship, chief of which are: (i) gross lithology, shales compacting quickly compared to sandstones, (ii) depositional facies, which controls grain size, sorting and clay content and therefore initial (surface) porosity, (iii) composition of framework grains: for example, pure quartz arenites differ from lithic arenites containing ductile fragments, (iv) temperature strongly affects chemical diagenesis, such as quartz cementation, clay mineral growth, and pressure solution, and (v) time: porosity loss may require sufficiently long periods of time. The simplest trend recognized between porosity and depth is a linear trend of the form

$$\phi = \phi_0 - ay \tag{9.15}$$

where ϕ and ϕ_0 are the porosity at depth y and the initial porosity respectively, and a is an empirically derived coefficient. This linear relationship appears to fit data carefully chosen from specific sedimentary facies within a certain formation of given geological age from one basin, for example, cross-stratified, massive, and ripple cross-laminated sandstones of the Jurassic Etive Formation of the North Sea (Fig. 9.1a). In this example, the slope of the linear regression gives $a = 0.09\,\text{km}^{-1}$. However, a linear relationship self-evidently cannot apply at large depths, since porosities would have to become negative. A more widely used porosity–depth relation therefore has

the form of a negative exponential (Athy 1930; Hedberg 1936), which produces an asymptotic low porosity with increasing depth. For normally pressured sediments, the variation of porosity ϕ with depth y is given by

$$\phi = \phi_0 e^{-cy} \tag{9.16}$$

where c is a coefficient determining the slope of the ϕ-depth curve, y is the depth, and ϕ_0 is the porosity at the surface. In other words, the surface porosity declines to $1/e$ of its original surface value at a depth of $1/c$ km (Fig. 9.2). On a depth versus log porosity graph, the value of c is the inverse of the rate of change of porosity with depth. The coefficient c can therefore be estimated if a number of porosity measurements can be made, for example from a sonic log from a representative borehole in the basin. This relationship has been applied to a range of different lithologies, each with its own value of c (Sclater and Christie 1980; Halley and Schmoker 1983) (Table 9.1) (Fig. 9.3).

Substituting (9.7) into (9.16) to eliminate depth y,

$$\phi = \phi_0 \exp\left[-\left\{\frac{c}{(\bar{\rho}_b - \rho_w)g}\right\}\sigma_{eff}\right] \tag{9.17}$$

where σ_{eff} is the vertical effective stress, equal to the overburden stress minus the pore pressure. This equation expresses a fundamental relation between the effective stress on sediment grains and the resultant porosity. However, it is difficult to solve since the bulk density of the water-saturated sediment column $\bar{\rho}_b$ is itself a function of the porosity ϕ. If we simply state that the effective stress driving compaction is a linear function of depth, equation (9.16) simplifies to

$$\phi = \phi_0 \exp[-c_2\sigma_{eff}] \tag{9.18}$$

where c_2 is a composition- and temperature-dependent coefficient derived for each lithology or facies under consideration. In normally pressured basins at depths of >1 km, where the lithostatic (overburden) and pore

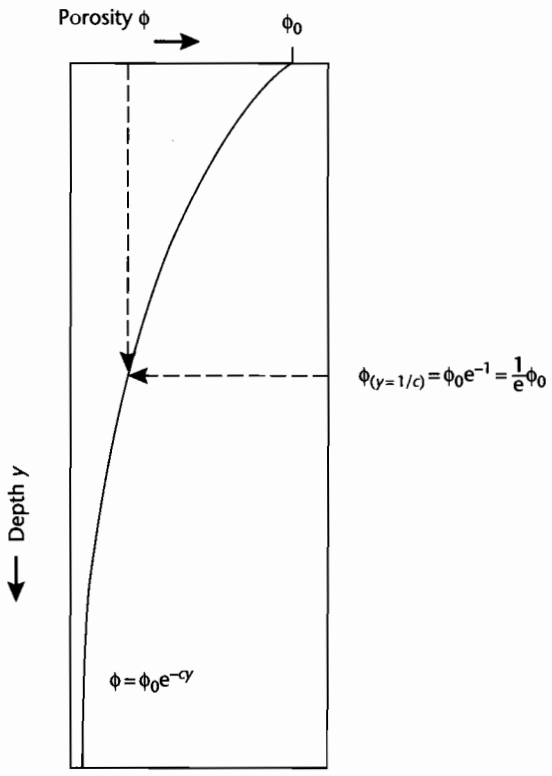

Fig. 9.2 Schematic diagram illustrating the use of the porosity–depth coefficient c. If a porosity–depth curve is known and it is exponential, c can be found by determining the depth at which the porosity ϕ has decreased to 1/e of its surface value ϕ_0. This should be repeated for all lithologies.

Table 9.1 Exponents used by Sclater and Christie (1980) for different lithologies in the subsurface of the North Sea.

Lithology	Surface porosity ϕ_0	Porosity–depth coefficient c (km^{-1})	Sediment grain density ρ_{sg} (kg m^{-3})
Shale	0.63	0.51	2720
Sandstone	0.49	0.27	2650
Chalk	0.70	0.71	2710
Shaly sandstone	0.56	0.39	2680

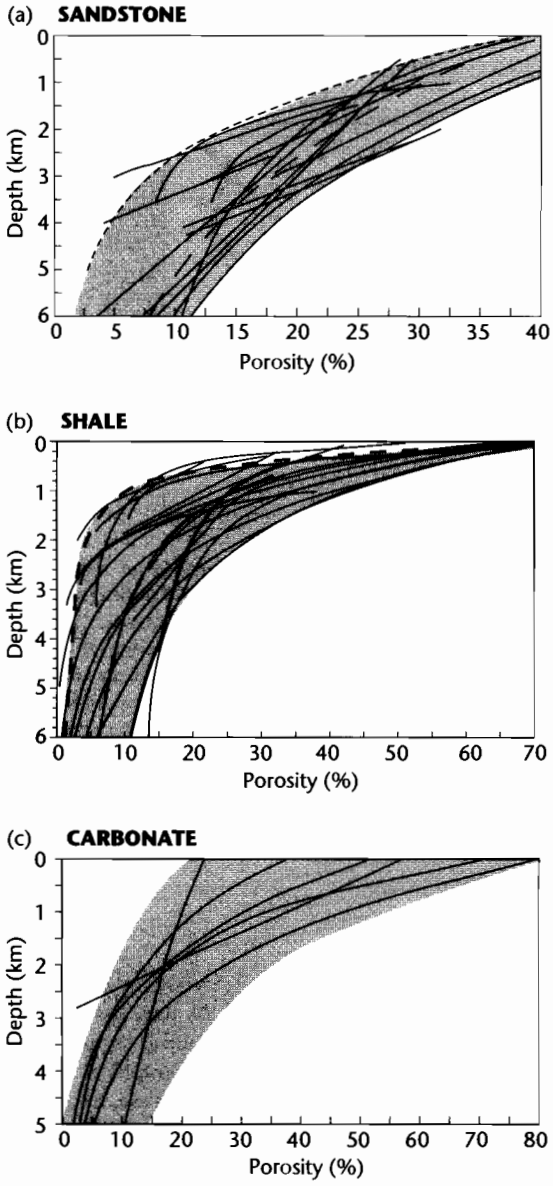

Fig. 9.3 Compilation of porosity–depth curves for sandstones (a), shales (b), and carbonates (c). Sources of datasets in Giles (1997). Note that shales compact early compared to sandstones. The porosity–depth relation for carbonates varies according to grain types and amount of cementation. Reproduced courtesy of Springer.

fluid pressure gradients are roughly constant, the porosity can be expressed

$$\phi = \phi_0 \exp\{-c_2(s-p)y\} \tag{9.19}$$

It has been argued that the exponential porosity–depth relationship does not fit shallower depth data particularly well (Falvey and Middleton 1981; Falvey and Deighton 1982). An alternative general porosity–depth function is based on the assumption that an incremental change in porosity is proportional to the change in the load and the ratio of void space to skeletal (grain) volume. This relationship is given by

$$1/\theta = 1/\theta_0 + c_3 y \tag{9.20}$$

where c_3 is a coefficient again related to lithology.

Baldwin and Butler (1985) expressed the porosity loss with depth in terms of the solid rock volume S, equivalent to $1-\phi$:

$$S = 1-\phi = 1-a\exp(-by) \tag{9.21}$$

where a and b are coefficients equal to 0.49 and 0.27 for sandstones and y is measured in kilometers. It can immediately be seen that this is the familiar exponential porosity–depth relation proposed by Athy (1930). For mudstones, Baldwin and Butler (1985) suggest an expression that can be modified to

$$\phi = 1-S = 1-ay^b \tag{9.22}$$

where a and b are 0.75 and 0.16 respectively for mudstones <200 m thick, which are thought to be normally pressured, and 0.71 and 0.125 for thicker mudstone sections that may develop overpressures.

In overpressured sections the effective stress–porosity equation can be modified by use of the ratio between fluid pressure and overburden pressure λ. This gives

$$\phi = \phi_0 \exp\left[-c\left\{\frac{\overline{\rho}_b(1-\lambda)y}{(\overline{\rho}_b-\rho_w)}\right\}\right] \tag{9.23}$$

The example from a North Sea borehole shown in Figure 9.4 illustrates the effect of overpressuring on the porosity–depth curve.

The evolution of porosity with depth can also be investigated in a physically more meaningful way by using Audet and McConnell's (1992, 1994) sedimentation parameter α. Numerical solution of the equation governing the evolution of porosity as a function of depth below the depositional surface d and time t, as a function of the sedimentation parameter, shows that clay strength (compressibility) and permeability (hydraulic conductivity) strongly affect overpressure and the evolution of porosity in a sedimentary basin. The curve of porosity versus depth is strongly affected by the sedimentation parameter (Fig. 9.5). As α varies from 1 to 10, the sediment becomes more compacted at a given depth d. This is because at $\alpha = 10$ pore fluid is easily expelled, leading to near hydrostatic pore fluid pressures and significant compaction, whereas when $\alpha = 1$ pore fluid motion is inhibited, causing reduced porosity loss in the sediment.

Some porosity–depth relationships are entirely based on the statistical analysis of large numbers of samples derived from different depths and known or "normal" geothermal gradients (Dzevanshir et al. 1986; Scherer 1987). Although potentially useful, these multivariate regressions lack any underlying physical principles.

In summary, there is a proliferation of porosity–depth relations, each based on a similar principle of porosity destruction under the increasing effective stresses experienced during burial, but differing in detail. It seems likely that each "standard" porosity–depth curve may be valuable if carefully calibrated and then used only within the region of calibration. For example, coefficients in the expressions should be evaluated for carefully selected porosity data in which grain size/sorting, composition, geothermal gradient and geological age are constrained.

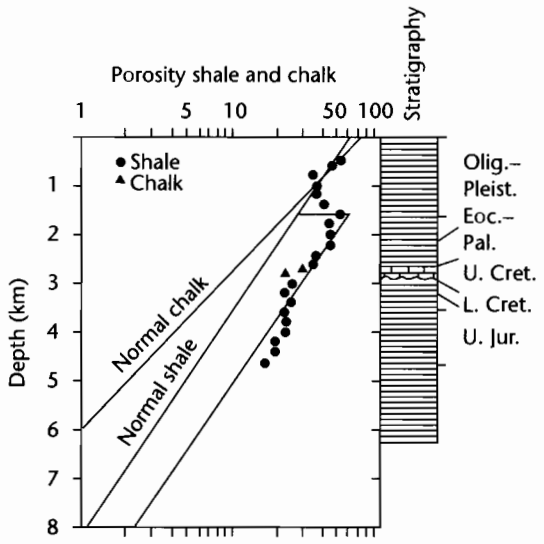

Fig. 9.4 Estimated porosity versus depth for an overpressured borehole in the Central Graben of the North Sea (Amoco 2/11-1). The increase in estimated porosity between 1500 and 2000 m is thought to be due to overpressuring. It causes a marked offset of the exponential segments of the porosity–depth curves (after Sclater and Christie 1980). The porosity–depth curves were calculated assuming total sealing occurred at the end of the Eocene, with overpressured units below and normally pressured above. The wavy line in the stratigraphic column represents the Albian–Aptian unconformity.

9.2.5 Decompacted thicknesses

To calculate the thickness of a sediment layer at any time in the past, it is necessary to move the layer up the appropriate porosity–depth curve: this is equivalent to sequentially removing overlying sediment layers and allowing the layer of interest to decompact. In so doing, we keep mass constant and consider the changes in volumes and therefore thicknesses (Boxed text 9.1).

Alternative porosity–depth relationships can be used as the basis for decompaction exercises. For example, Falvey and Middleton's (1981) formulation is used to calculate decompacted thicknesses in Allen and Allen (1990, p.270).

Equation (9.30) calculates the thickness of a sediment layer at any time from the point of deposition to the present day. A decompacted subsidence curve can therefore be plotted. The sources of the data points of the subsidence curve are the stratigraphical boundaries of presumed known age defining stratigraphical units of known present-day thickness. All depths are, however, in relation to a present-day datum, normally taken as mean sea level. Consequently it is necessary to correct the decompacted subsidence curve for firstly the difference in height between the depositional surface and the regional datum (*paleobathymetric correction*), and secondly, for past variations in the ambient sea level compared to today's (*eustatic correction*). Finally, the sediment weight drives basement subsidence. In order to calculate the true tectonic subsidence, it is necessary to remove the effects of the excess weight of the sediment compared to water. This is known as *backstripping* (§9.3).

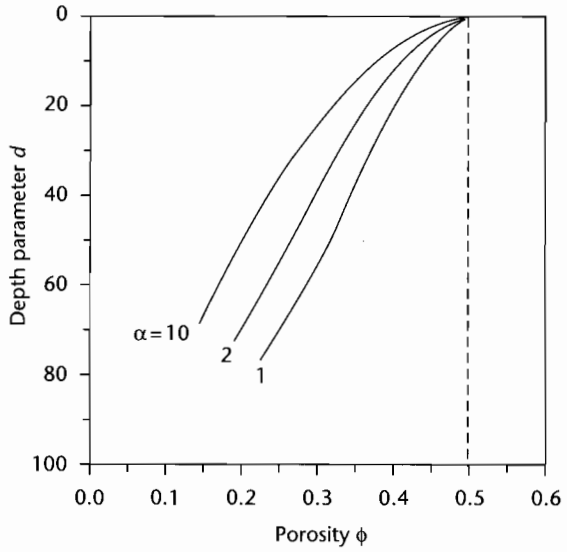

Fig. 9.5 Effect of the sedimentation parameter α on the porosity–depth curve. Porosity is shown versus a dimensionless depth for a time corresponding to 20 Myr after the start of gravitational compaction. For the parameter values used to calculate the porosity–depth curves, $d = 10$ corresponds to *c.* 1 km burial depth, and maximum burial depths are 7–8 km. Note that at high values of the sedimentation parameter α, the curve is "normal" or hydrostatic, with increasing effects of overpressuring at lower values of α. The initial porosity ϕ_0 is 0.5. After Audet and McConnell (1992). Reproduced courtesy of Blackwell Publishing Ltd.

9.3 SUBSIDENCE HISTORY AND BACKSTRIPPING

In the previous section we saw how it was possible to account for the progressive compaction of a sedimentary column during burial in a sedimentary basin. The decompacted sediment thicknesses allow a graph of *sediment accumulation rate* versus time to be constructed. However, this sediment accumulation rate graph is not the same as the subsidence rate of a chosen geological horizon relative to a constant datum. Nor does it directly give us the magnitude of the tectonic driving force as a function of time. To gain insights into subsidence rate and tectonic driving force we need to make a number of modifications or "corrections" to the sediment accumulation rate curve derived by decompaction of the stratigraphic column. In this section we perform these modifications on a 1-D stratigraphic column. In §9.4 we briefly consider the use of 2-D and 3-D models.

9.3.1 Paleobathymetric corrections

The estimation of water depth for a given stratigraphic horizon is generally far from easy, yet it is essential in order to accurately study subsidence history. As an example of the potential problems, consider two sedimentary basins (a) and (b) (Fig. 9.7). In basin (a) the water depth is 5 km. If the basement subsides tectonically by 1 km over a certain time period and during this time sediment is supplied to the basin such that it becomes filled to the brim, local isostasy shows that

BOXED TEXT 9.1: Decompaction

Consider a sediment layer at present depths of y_1 and y_2 which is to be moved vertically to new shallower depths y'_1, and y'_2 (Fig. 9.6). From equation (9.16) the amount of water-filled pore space V_w between depths y_1 and y_2 is simply the porosity integrated over the depth interval,

$$V_w = \int_{y_1}^{y_2} \phi_0 e^{-cy} dy \qquad (9.24)$$

which on integration gives

$$V_w = \frac{\phi_0}{c}\{\exp(-cy_1) - \exp(-cy_2)\} \qquad (9.25)$$

Since the total volume of the sediment layer (V_t) is the volume due to pore-filling water (V_w) and the volume of the sediment grains (V_s),

$$V_s = V_t - V_w \qquad (9.26)$$

and from (9.25), considering a unit cross-sectional area,

Continued

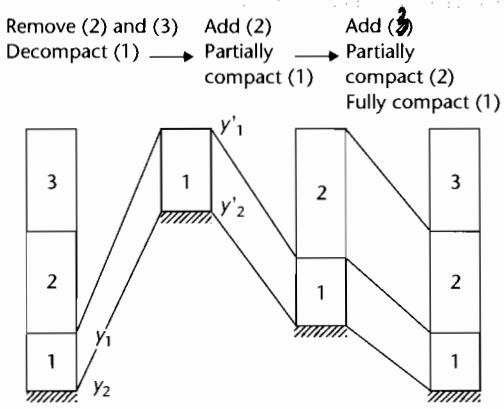

Fig. 9.6 Concept of the successive stages in a decompaction exercise.

$$y_s = y_2 - y_1 - \frac{\phi_0}{c}\{\exp(-cy_1) - \exp(-cy_2)\} \qquad (9.27)$$

On decompaction the sediment volume remains the same, only the volume of water expanding. The height of the water in a unit area sedimentary column lying between depths y'_1, and y'_2 is from (9.25)

$$y'_w = \frac{\phi_0}{c}\{\exp(-cy'_1) - \exp(-cy'_2)\} \qquad (9.28)$$

The new decompacted thickness of the sediment layer is the sum of the thickness due to the sediment grains (9.27) and that due to the water (9.28). That is,

$$y'_2 - y'_1 = y_s + y'_w \qquad (9.29)$$

which becomes

$$y'_2 - y'_1 = y_2 - y_1 - \frac{\phi_0}{c}\{\exp(-cy_1) - \exp(-cy_2)\} + \frac{\phi_0}{c}\{\exp(-cy'_1) - \exp(-cy'_2)\} \qquad (9.30)$$

This is the general decompaction equation. It represents mathematically the exercise of sliding the sediment layer up the exponential porosity–depth curve. Its solution is by numerical iteration, which makes it ideal for solving by computer. A Matlab decompaction program is provided on the web site www.erdw.ethz.ch/Allen.

about 15 km of sediment will have accumulated at the end of the time period. In basin (a), therefore, a stratigraphic thickness of 15 km reflects a very small (1 km) driving subsidence. In basin (b), however, a tectonic subsidence of 1 km takes place in a basin that has its depositional surface already at sea level. The resultant sediment thickness is barely 3 km at the end of the same time period. Clearly, for the same rate of tectonic subsidence, enormously different stratigraphic thicknesses can result depending on the initial and ensuing paleobathymetry.

Information on paleobathymetry comes from a number of sources, chief of which are benthic microfossils, other faunal and floral assemblages, sedimentary facies, and distinctive geochemical signatures. Without paleontology, it is very difficult to constrain paleobathymetry. A recent compilation of papers illustrating the use of micropaleontological data in assessing sea-level change and stratigraphic architectures is found in Olson and Leckie (2003).

Although some organisms inhabit a particular depth range as an adaptation to hydrostatic pressure, most paleodepth estimates are indirectly obtained. For example, qualitative estimates can be obtained by a comparison with the modern occurrences of certain species or assemblages and by recognition of the ecological trends of benthonic and planktonic organisms through time. Estimates can also be obtained by quantitative methods, using ratios of, for example, plankton/benthos, arenaceous/calcareous foraminifers, percent radiolarians or ostracods, or alternatively using species dominance and diversity, morphological characters and so on. These many techniques allow the paleontologist to make meaningful interpretations of environmental factors such as the chemical environment (salinity, pH, oxygen and CO_2 contents, nutrient availability), the physical environment (temperature, light, energy level, type of substrate, turbidity), and the biological environment. As much information as possible needs to be synthesized to produce a reliable depth estimate. An early example given in Figure 9.8 shows the type of depth information that can be obtained paleontologically, together with the ranges over which the estimate may span.

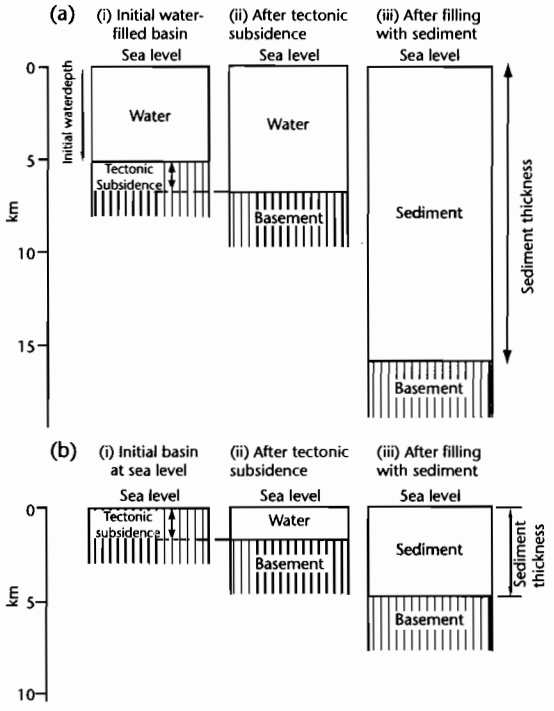

Fig. 9.7 Schematic illustration of the effects of initial water depth on sediment thickness. (a) Sedimentary basin with an initial water depth of 5 km (i) undergoes 1 km of tectonic subsidence (ii) and is filled with sediment to a depth of 15 km (iii); (b) Sedimentary basin initially at sea level (i) undergoes 1 km of tectonic subsidence (ii) and accumulates *c.* 3 km of sediment (iii).

Sedimentary and geochemical data are, by comparison, far less useful. Sedimentary facies reflect supply and process and are not therefore particularly diagnostic of depth. Although some structures, such as wave ripple marks, are restricted to particular depth ranges (<200 m), the sedimentary facies more likely will provide a back-up to the paleontological observations in marine sediments. In continental environments the potential for using sedimentary facies is greater. If shoreline facies can be identified for example, the calculation of floodplain slopes from fluviatile sediments can give valuable information on heights above sea level (Fasel 1986; Homewood et al. 1986). The most obvious geochemical data relate to the depth of carbonate dissolution (CCD) below which calcareous material is dissolved. Because most of this material is in the form of calcareous microfossils, it falls within the realm of the paleontologist. Some mineral species such as glaucony and phosphates may provide useful information on paleowater depth, but estimates are likely to be far from precise.

9.3.2 Eustatic corrections

The concept of sea-level change relative to a reference datum is known as *eustasy*, and the absolute, global sea-level variation relative to this reference datum is a eustatic change. We saw in §8.3.4 that any increase (or decrease) of water in the ocean must be compensated isostatically. If an ocean with initial water depth h_1 is filled with water to a new depth h_2, the sea-level rise Δ_{SL} compensated for isostatic depression of the ocean floor is

$$\Delta_{SL} = \left(\frac{\rho_m - \rho_w}{\rho_m}\right)(h_2 - h_1) \tag{9.31}$$

The new elevation of sea level relative to a sea level datum, caused by an increase in the water column h, termed *freeboard*, is therefore simply

$$f = \frac{(\rho_m - \rho_w)h}{\rho_m} \tag{9.32}$$

Inserting reasonable values for the density terms for an oceanic basin ($\rho_m = 3300\,\mathrm{kg\,m^{-3}}$ and $\rho_w = 1030\,\mathrm{kg\,m^{-3}}$) gives $f = 0.69h$.

At present, there is no consensus on a global eustatic curve that could be used to make corrections of decompacted subsidence data in order to extract the tectonic subsidence. Backstripping is required to remove the effects of sediment loading from observed basin subsidence (see §9.3.3). To extract the eustatic signal from the backstripped subsidence curve, the component due to tectonics must be identified and removed. However, this is not known and must be inferred or modeled. Detailed analysis of a number of borehole records from the Atlantic coastal plain in northeastern USA and the adjacent continental slope has used a tectonic model of slow cooling following rifting, to isolate the eustatic component (Miller et al. 1998). The long-term eustatic curves for the Cenozoic, which show a long term lowering of 150–200 m since 65 Ma, are similar to the estimates

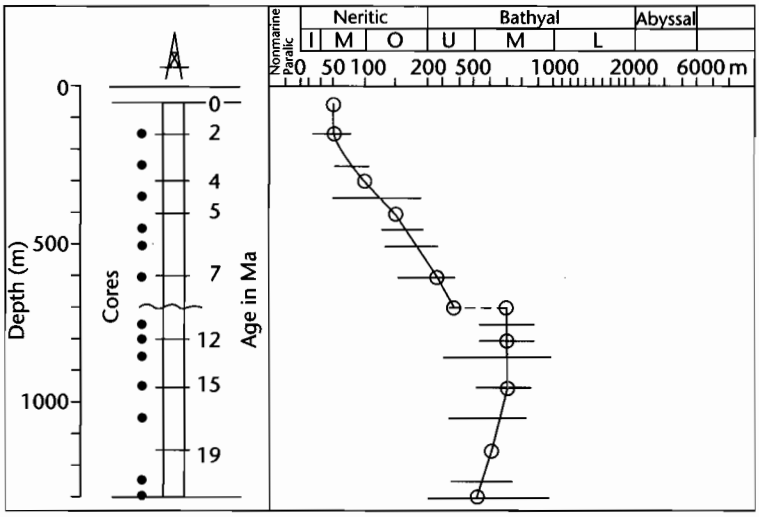

Fig. 9.8 An early example of the use of micropaleontological data to estimate paleobathymetric changes through time (after van Hinte 1978). Dots indicate core data, from which paleobathymetric estimates are made. As much paleontological information as possible is used to guide the choice of the position of the paleobathymetric curve through the depth ranges indicated by the horizontal lines. The midpoints of the ranges need not be used.

based on ocean ridge volume changes (Pitman 1978; Kominz 1984), but substantially less than the Haq et al. (1987) estimate of a *c.* 300 m lowering (Fig. 8.31). Shorter term eustatic changes are more difficult to extract. Short-term eustatic height changes are <50 m – similar to those derived from oxygen isotope records (Miller et al. 1991) but once again somewhat lower than the *c.*50–100 m estimates of Haq et al. (1987).

Bearing in mind these uncertainties, it is advisable firstly to decompact ignoring any possible global sea-level fluctuations. Following this, the sea level changes associated with first-order (long-term) cycles can be included, following Kominz (1984), Kominz et al. (1998) and Miller et al. (1998). The amplitudes of long-term eustatic change in Haq et al. (1987) are too high by a factor of about 2. It is not advisable to *a priori* invoke the short term eustatic excursions proposed by Haq et al. (1987).

9.3.3 Backstripping the sediment load

The sediment and water load above a horizon of interest in a sedimentary basin causes an isostatic effect so that the total subsidence observed is made of a tectonic driving force component and a sediment/water load component. Watts and Ryan (1976) were the first to propose the isolation of the tectonic driving force by removal of the isostatic effects of the sediment load and called the technique *backstripping*. Backstripping using Airy isostasy is shown in Boxed text 9.2.

9.3.4 Flexural support for sediment loads

Since the lithosphere underlying sedimentary basins has flexural strength, it is likely that sediment loads of appropriate wavelength are compensated flexurally rather than in a local Airy fashion. In order to understand the principle of flexural backstripping we return to the problem of the deflection of the lithosphere under a periodic load found in §2.3.3. The degree of compensation for a periodic load (eqn 2.84) is determined principally by the flexural rigidity D and the wave number $2\pi/\lambda$. The relationship between degree of compensation and wave number is shown in Figure 2.27. Taking the fill of a sedimentary basin 200 km wide ($\lambda/2 = 200$ km) with a

BOXED TEXT 9.2: Backstripping

At its simplest, the influence of the sediment load can be evaluated as follows. The porosity of the sediment layer at its new depth is

$$\phi = \frac{\phi_0}{c} \cdot \frac{\exp(-cy_1') - \exp(-cy_2')}{y_2' - y_1'} \tag{9.33}$$

Since the bulk density of the new sediment layer (ρ_b) depends on the porosity and the density of the sediment grains (ρ_{sg})

$$\rho_b = \phi\rho_w + (1-\phi)\rho_{sg} \tag{9.34}$$

the bulk density of the entire sedimentary column ($\bar{\rho}_b$) made up of i layers is

$$\bar{\rho}_b = \sum_i \left\{ \frac{\bar{\phi}_i\rho_w + (1-\bar{\phi}_i)\rho_{sgi}}{S} \right\} y_i' \tag{9.35}$$

where $\bar{\phi}_i$ is the mean porosity of the ith layer, ρ_{sgi} is the sediment grain density of the same layer, y_i' is the thickness of the ith sediment layer, and S is the total thickness of the column corrected for compaction.

The loading effect of the sediment can then be treated as a problem of a local (Airy) isostatic balance. Where sediment is replacing a column of water,

$$Y = S\left(\frac{\rho_m - \bar{\rho}_b}{\rho_m - \rho_w}\right) \tag{9.36}$$

where Y is the depth of the basement corrected for sediment load and ρ_m, $\bar{\rho}_b$, ρ_w are mantle, mean sediment column, and water densities.

Incorporating the various effects of paleobathymetry, eustatic sea-level change, and sediment loading gives the Airy compensated tectonic subsidence

$$Y = S\left(\frac{\rho_m - \bar{\rho}_b}{\rho_m - \rho_w}\right) - \Delta_{SL}\left(\frac{\rho_w}{\rho_m - \rho_w}\right) + (W_d - \Delta_{SL}) \tag{9.37}$$

where Δ_{SL} is the paleosea level relative to the present, and W_d is the paleowater depth (Bond and Kominz 1984). This is the subsidence relative to a stationary datum (today's sea level) that would have occurred in an entirely water-filled basin. An example of a decompacted, corrected, and backstripped subsidence history is given in Fig. 9.9.

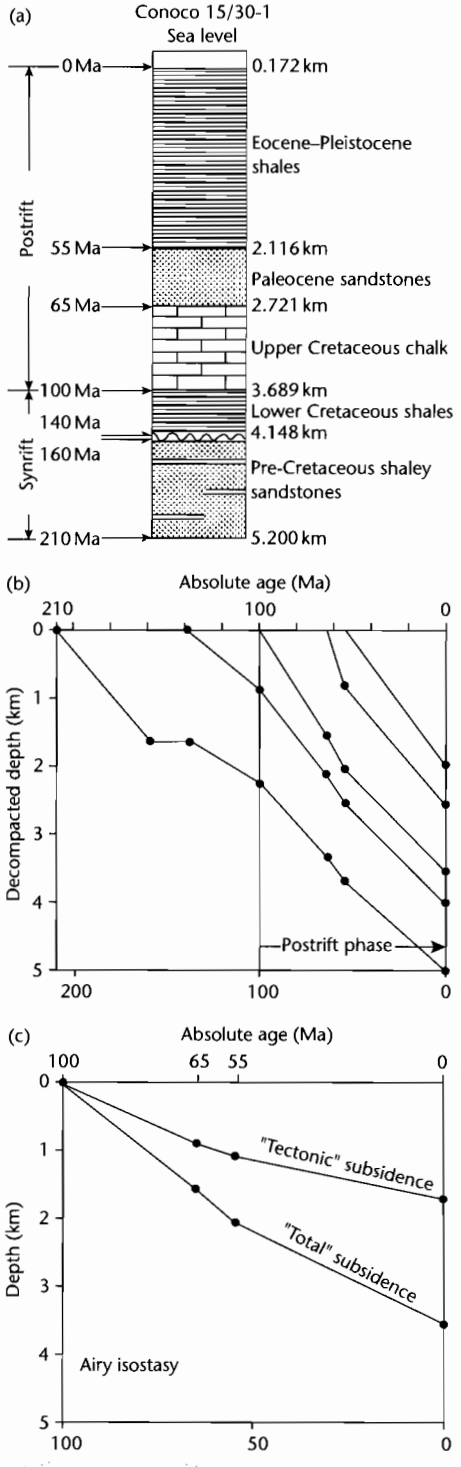

Fig. 9.9 Example of a decompaction and backstripping of the stratigraphy penetrated in a North Sea borehole, Conoco 15/30-1. (a) Summary stratigraphic column, (b) decompacted depth versus time, (c) backstripped subsidence for the postrift phase, using an Airy isostatic model and eustatic and paleobathymetric corrections at 100 Ma, 65 Ma, 55 Ma, and 0 Ma. Full dataset and Matlab exercise is provided at www.erdw.ethz.ch/Allen

sinusoidal sediment load and an underlying lithosphere of flexural rigidity 10^{24} Nm, $(\rho_m - \rho_s) = 800\,\mathrm{kg\,m^{-3}}$, the degree of compensation C is about 0.12. This suggests that the lithosphere behaves very rigidly to this kind of wavelength of load. Changing the wavelength of the load such that $l/2$, the width of the basin, is now 400 km, C = 0.68, indicating that the sediment load is only weakly supported. In this case of large compensation, Airy-type isostasy is approached.

Flexural backstripping can therefore only be carried out if there is knowledge of the flexural rigidity of the underlying lithosphere and of the spatial distribution of the sediment load. The procedure is normally carried out sequentially on a number of sediment layers where the isopachs of each layer are known from seismic reflection data. The flexure is then given by

$$\mathbf{Y}(k) = \frac{(\rho_s - \rho_w)\mathbf{S}(k)}{(\rho_m - \rho_s)}\mathbf{\Phi}(k) \tag{9.38}$$

where $\mathbf{Y}(k)$ is the frequency domain equivalent of the flexure, $\mathbf{S}(k)$ is the frequency domain equivalent of the sediment thickness, and $\mathbf{\Phi}(k)$ is a wave number function equivalent to the compensation C outlined above.

Flexural backstripping can be extended to three dimensions by replacing the wave number by a 3-D wave number

$$k = \sqrt{(k_x^2 + k_z^2)} \tag{9.39}$$

where k_x is the wave number in the x direction and k_z is the wave number in the z direction.

An example of the use of flexural backstripping from the Valencia Trough of the western Mediterranean is given in Figure 9.10.

9.3.5 Tectonic subsidence signatures

One of the benefits of a complete decompaction and backstripping procedure is that the subsidence history of basins can be compared without the complications of different paleobathymetric, eustatic, compactional, and isostatic effects. This enables the tectonic driving force for subsidence, for example, the stretch factor β, to be evaluated at different positions within a single basin, and for the same tectonic mechanism to be compared between different basins. It also enables the tectonic subsidence history of sedimentary basins to be discriminated and compared with theoretical curves.

Stretching of the continental lithosphere and flexure of the lithosphere are by far the most important mechanisms for prolonged and widespread subsidence. Stretching and flexure produce entirely different subsidence profiles:

1 Stretching of the continental lithosphere produces a rapid synrift subsidence followed by an exponentially decreasing postrift subsidence due to thermal relaxation. Although a range of subsidence history possibilities arise from the duration of the stretching, 3-D heat flow, induced convection in the zone of upwelled asthenosphere, maintenance or removal of a hot source in the mantle, lateral relay during simple shear, and depth-dependent stretching, nevertheless the diagnostic signature of continental stretching is an early, rapid, fault-controlled phase of subsidence followed by a "concave-up" phase as the lithosphere cools. The amount of synrift and postrift subsidence depends essentially on the amount of stretching β.

2 Flexure of the lithosphere under a moving load, such as an orogenic wedge, typically produces an accelerating subsidence through time. This is the simple result of the propagation of a flexural wave with a maximum deflection under the load across the lithosphere. Consequently, locations on the foreland plate distant from the load are initially uplifted in a forebulge region, producing an unconformity, and then subside at an increasing pace as they become involved in foredeep subsidence. The magnitude and geometry of the flexural subsidence depend on the flexural rigidity of the underlying plate and the magnitude and spatial distribution of the applied load.

The typical subsidence signatures of stretched basins and foreland basins are compared in Figure 9.11(a, b). A first-order conclusion from such a comparison is that: (i) stretched basins contain rift to postrift megasequences with a duration of $10^1 - >10^2$ Myr, with synrift tectonic subsidence rates of typically $<0.2\,\mathrm{mm\,yr^{-1}}$ and exponentially decreasing postrift tectonic subsidence rates of $<0.05\,\mathrm{mm\,yr^{-1}}$, and (ii) foreland basin megasequences are typically 20–40 Myr in duration and involve convex-up subsidence signatures with maximum tectonic subsidence rates of 0.2–0.5 $\mathrm{mm\,yr^{-1}}$. Thicknesses of foreland

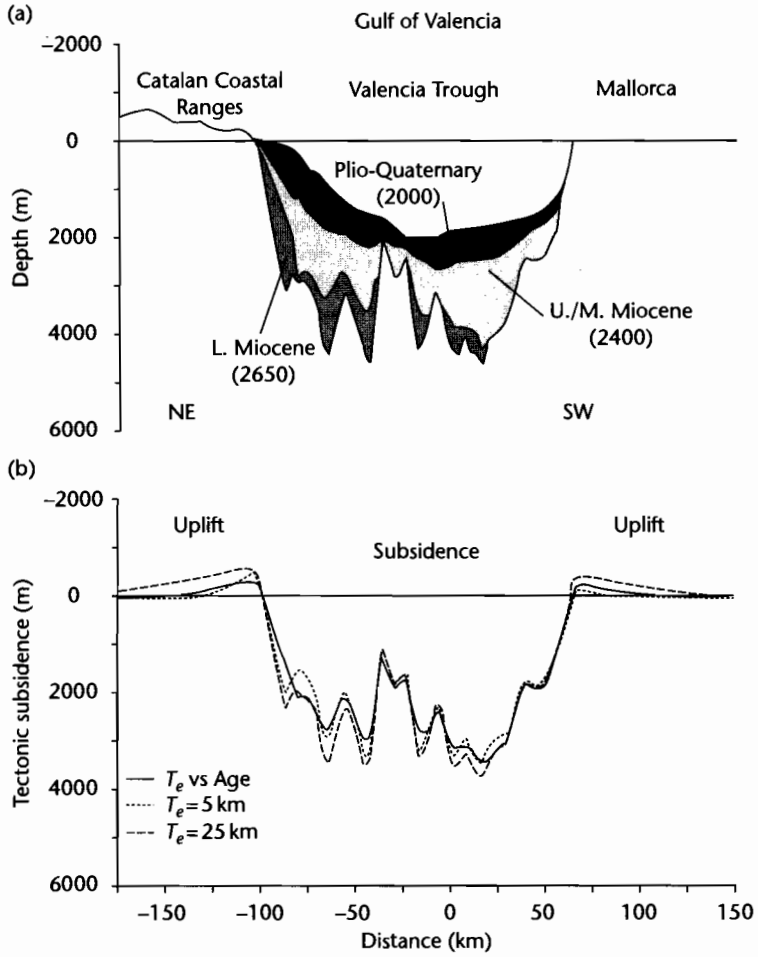

Fig. 9.10 Application of flexural backstripping technique to the Valencia Trough, a young rift basin in the western Mediterranean between the Spanish mainland and the Balearic Islands, that extended in the early Miocene. (a) Stratigraphic cross-section with estimated densities (in $kg\,m^{-3}$) of the Plio-Quaternary, upper/middle Miocene and lower Miocene; (b) Backstripped tectonic subsidence using three models for the equivalent elastic thickness. After Watts and Torné (1992b). Reproduced courtesy of American Geophysical Union.

basin stratigraphy range up to 10 km. Cratonic basins are typified by very long periods ($>10^2$ Myr) of slow subsidence interrupted by regional unconformities, with tectonic subsidence rates of $0.01–0.04\,mm\,yr^{-1}$. Strike–slip basins may be particularly difficult to discriminate on the basis of tectonic subsidence signature, since basins in strike–slip zones are strongly related to the kinematics of border fault movement. Basins may have components of thermal relaxation, lateral heat loss, and flexure from nearby push-up ranges contributing to the tectonic subsidence signature. Tectonic subsidence rates are commonly very high compared to all other basin types ($>0.5\,mm\,yr^{-1}$), but strike–slip megasequences may be short in duration (*c.* 10 Myr) due to the complexities of deformation within the Principal Displacement Zone.

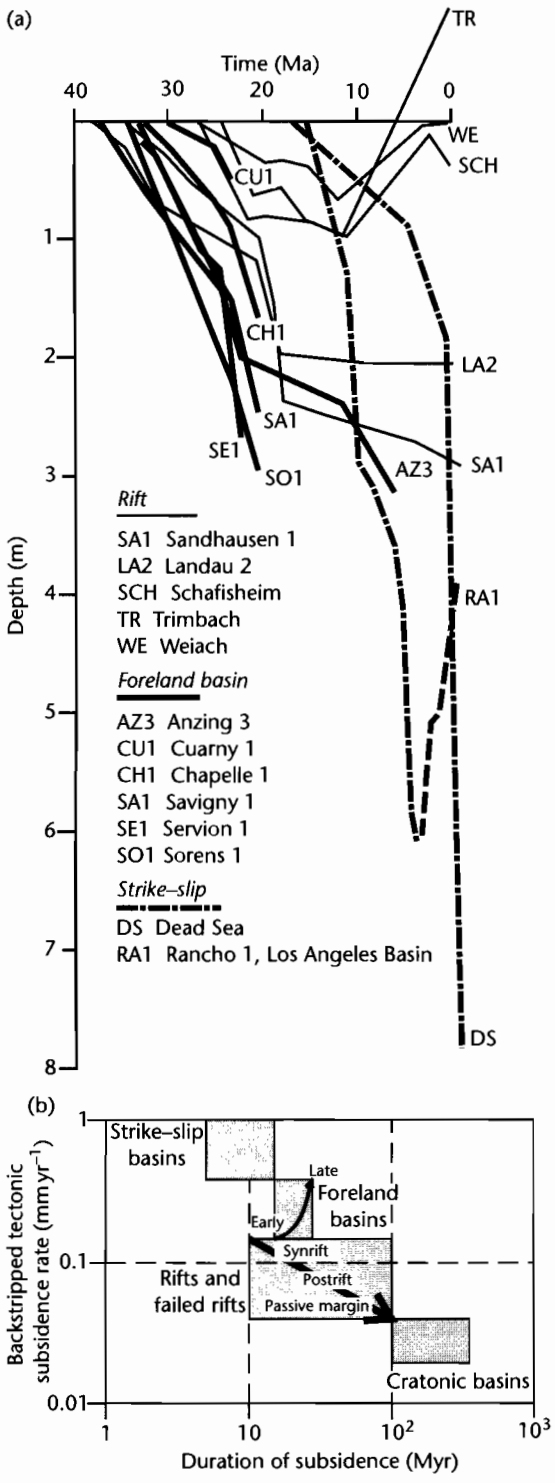

In many basins more than one subsidence mechanism may operate. This may be particularly the case in the retro-foreland regions of major ocean–continent convergence zones. In these regions flexural subsidence due to loading in retro fold and thrust belts may be added to by dynamic subsidence associated with subduction of cold oceanic slabs. Allen et al. (2000), for example, recognized two convex-up flexural events superimposed on a very long-term, linear to slightly concave-up subsidence curve in the Mesozoic of the Colorado Plateau area, USA. The addition of an in-plane stress related to continental collision to the postrift history of stretched basins may also be recognized by "anomalous" increases in subsidence rate. This combination of mechanisms has been invoked, for example, in the Late Cenozoic history of the North Sea failed rift (van Wees and Cloetingh 1996).

9.4 INTRODUCTION TO THERMAL HISTORY

Subsidence in sedimentary basins causes material initially deposited at low temperatures and pressures to be subjected to higher temperatures and pressures. Sediments may pass through diagenetic, then metamorphic regimes and may contain indices of their new pressure–temperature conditions. Thermal indices are generally obtained from either dispersed organic matter, temperature-dependent chronometers such as apatite fission tracks or from mineralogical trends. A great deal of effort has been spent in attempting to find an analytical technique capable of unambiguously describing thermal maturity, and an equal amount of effort attempting to correlate the resulting proliferation of indicators.

Numerical values of the organic geochemical parameters are dependent on time, thermal energy, and type

Fig. 9.11 Comparison of the typical subsidence histories of foreland basins, rift and strike–slip basins, using decompacted subsidence curves (a). Thick solid curves are boreholes in the flexural North Alpine foreland basin of Switzerland and southern Germany. Thin solid curves are the Tertiary rift phase of boreholes in the Rhine rift and its southerly continuation in northern Switzerland. The Swiss boreholes (TR, WE and SCH) have experienced Neogene uplift. Dash-dot lines are two strike–slip basins; (b) Plot of duration of subsidence versus typical tectonic subsidence rate, allowing foreland basins, rift, failed rift, passive margin and strike–slip basins to be discriminated.

of organic matter (e.g., Weber and Maximov 1976 for an early contribution). The evolution of clays and other minerals is controlled by temperature and by chemical and petrological properties. The scale of maturation to which a given organic or mineralogical phase can be calibrated is that of *coal rank*. Any analytical technique must be able to make use of very small amounts of dispersed organic matter in order to be valuable in basin analysis. Vitrinite reflectance and elemental analyzes enable coal rank to be related to hydrocarbon generation stages. Thermochronological tools such as apatite fission track analysis and the diffusion of He during U–Th decay offer the important advantage of providing information on thermal evolution instead of solely on maximum paleotemperature.

The objective in the remainder of this chapter is to describe the use of a number of thermal indicators in constraining and calibrating the thermal evolution of the basin-fill. The implications for the generation of hydrocarbons and for the diagenesis of reservoir rocks is developed in Chapter 10.

9.5 THEORY: THE ARRHENIUS EQUATION AND MATURATION INDICES

It is now believed that the effects of depth *per se* on the maturation of organic matter are of minor importance, the most important factors being *temperature* and *time*. Pressure is relatively unimportant. Philippi (1965) assessed the effect of pressure by studying hydrocarbons in two Californian basins. In the Los Angeles Basin, hydrocarbons were generated at about 8000 ft (~2.4 km) whereas in the Ventura Basin, generation did not take place until about 12,500 ft (3.8 km) of burial. Since pressure is directly related to depth of burial ($\sigma = \rho gh$) this suggests that pressure does not play a major part in hydrocarbon generation. However, the generation of hydrocarbons in the two basins took place at the same temperature, strongly suggesting that subsurface temperature was the overriding control.

The relationship between temperature and the rate of chemical reactions is given by the *Arrhenius equation*:

$$K = A\exp(-E_a/RT) \tag{9.40}$$

where K is the reaction rate, A is a constant sometimes termed the *frequency factor* (it is the maximum value that can be reached by K when given an infinite temperature), E_a is the activation energy, R is the Universal Gas Constant, and T is the absolute temperature in Kelvin. The constants in the Arrhenius equation can be estimated from compilations of organic metamorphism (e.g., Hood et al. 1975; Shibaoka and Bennett 1977). The activation energies of each individual reaction involved in organic maturation are not known, but for each organic matter type a distribution of activation energies may be established from laboratory and field studies. For example, a distribution of activation energies for the maturation of vitrinite from 159 to 310 kJ mol^{-1}, centered on 226 kJ mol^{-1}, was suggested by Burnham and Sweeney (1989).

The Arrhenius equation suggests that reaction rates should increase exponentially with temperature, so that a 10 °C rise in temperature causes the reaction rate to double. This result is widely known, but it is less widely realized that the rate of increase in reaction rate slows down with increasing temperature, so at 200 °C the reaction rate increases by a factor of 1.4 for a 10 °C rise in temperature (Robert 1988). Clearly, both time and temperature influence organic maturation, a view supported by the occurrence of shallower oil generation thresholds as the sediments containing the organic matter become older (Dow 1977) (Fig. 9.12). Connan (1974) believed that the threshold of the principal zone of oil generation was related to the logarithm of the age of the formation, further supporting a time–temperature dependence obeying the laws of chemical kinetics.

The cumulative effect of increasing temperature can be evaluated from the *maturation integral*, the reaction rate integrated over time,

$$C = A\int_0^t \exp(-E_a/RT) + C_0 \tag{9.41}$$

where C_0 is the original level of maturation of the organic material at the time of deposition ($t = 0$). The maturation integral for any nominated horizon can be calculated if the decompacted burial history, heat flow through time and thermal conductivities of the sediments and basement are known or can be assumed. For the less mathematically inclined, equation (9.41) shows that when paleotemperatures are plotted on an exponential scale, the area under the curve from deposition to a given time is proportional to the maturation integral at that time at the nominated horizon (plus the value of C_0) (see §9.6). Some authors believe that the maturation integral is related to measurable values of vitrinite reflectance (see §9.7.2, 9.8) (Royden et al. 1980; Falvey and Middleton 1981).

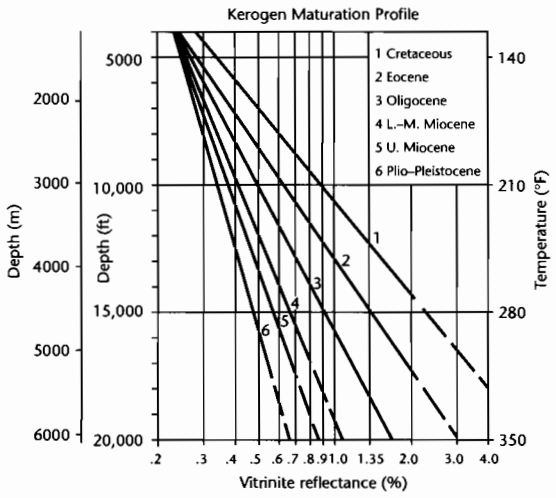

Fig. 9.12 Plot of depth versus an index of thermal maturation (vitrinite reflectance) for kerogens of various ages (after Dow 1977). For the same depth of burial (and therefore for the same temperature at a constant geothermal gradient), older kerogens are significantly more mature than younger kerogens.

Hood et al. (1975) devised an artificial maturation parameter, the *Level of Organic Metamorphism* (LOM), based on a rank progression of coals, from lignites to meta-anthracites. Hood's diagram shows the relationship between the "effective heating time" and the maximum temperature attained. The effective heating time is defined as the length of time the temperature remains within a 15 °C range of the maximum temperature. This method, although not stated explicitly by Hood et al. (1975), is based on the first-order chemical kinetics outlined above.

Another application of the Arrhenius relationship is the *Time–Temperature Index* (TTI) (Lopatin 1971; Waples 1980). This index is based on the view that the reaction rate doubles for every 10 °C rise in temperature over the entire range from 50 °C to 250 °C. Since the method assumes that the reaction rate continues to double over 10 °C intervals over the entire temperature range to 250 °C, it tends to overestimate maturity. The reaction cannot continue indefinitely because the materials undergoing thermal maturation are used up.

Other techniques, such as those of Tissot (1969), Tissot and Espitalié (1975), and Mackenzie and Quigley (1988), have been developed that enable masses of petroleum generated during thermal maturation of organic matter to be calculated. The Mackenzie and Quigley model is described in relation to petroleum source rocks in §10.3.2.2.

9.6 FACTORS INFLUENCING TEMPERATURES AND PALEOTEMPERATURES IN SEDIMENTARY BASINS

Chapter 2 contains some basic concepts about heat flow, and the specific problem of 1-D (vertical) heat flow in basins due to stretching is addressed in Chapter 3. Here, we are concerned with the various "internal" factors that influence the temperatures within sedimentary basins: (i) variations in thermal conductivity, (ii) internal heat generation, (iii) convective/advective heat transfer within sediments, and (iv) surface temperature changes.

9.6.1 Effects of thermal conductivity

The distribution of temperature with depth (geotherm) in the continents is primarily determined by conductive heat transport. We know the relation between heat flux and temperature gradient as given by Fourier's law (eqn 2.29). This law states that conductive heat flux is related to the temperature gradient by a coefficient, K, known as the coefficient of *thermal conductivity*. If two measurements of temperature are known, one T_y, at depth y and another T_0 at the surface ($y = 0$), Fourier's law can be restated as

$$q = -K(T_y - T_0)y \tag{9.42}$$

which by rearrangement becomes

$$T_y = T_0 + \left(\frac{-qy}{K}\right) \tag{9.43}$$

where q is the heat flux (negative for y increasing downwards). We are here initially ignoring internal heat production within the sedimentary pile (see §9.6.2).

Ignoring for the moment lithological variations, thermal conductivities of sediments vary as a function of depth because of their porosity loss with burial (§9.2).

Equation (9.43) can be modified to account for the different thermal conductivities of the sedimentary layers,

$$T_y = T_0 + (-q)\left\{\frac{l_1}{K_1} + \frac{l_2}{K_2} + \frac{l_3}{K_3} + \ldots\right\} \quad (9.44)$$

where l_1 to l_n are the thicknesses of the layers with thermal conductivities K_1 to K_n, and $l_1 + l_2 + l_3 \ldots$ must of course be equal to y.

Falvey and Middleton (1981) recommended the use of a function that assumed an exponental relation between porosity and depth

$$K = K_d - \{(K_d - K_0)\exp(-\gamma y)\} \quad (9.45)$$

where K_d is the thermal conductivity deep in the sedimentary section, K_0 that at the sediment surface, and γ is a constant for a given section. Since K varies with depth, temperature gradients must also vary with depth in order to maintain a constant heat flow. If present-day heat flow can be calculated from a borehole by measurement of conductivities and surface and bottom hole temperatures (§9.7.1), equations (9.43) and (9.45) can be used to find the temperature at any depth. If paleoheat flow is then assumed to be constant with depth, the temperature history of any chosen stratigraphic level can be estimated. The assumption of a constant heat flow with depth is a condition of any 1-D steady-state heat conduction model. Measurements in some sedimentary basins such as the North Sea failed rift (Andrews-Speed et al. 1984), however, suggest that this is not a good assumption, deep circulation of water most likely being responsible for the departure from the steady-state assumption (see §9.6.3).

A fundamental requirement in the estimation of geotherms, temperatures, and paleotemperatures in sedimentary basins is therefore the bulk thermal conductivity of the different sedimentary layers making up the basin-fill. Thermal conductivities can be measured in the laboratory (Carslaw and Jaeger 1959; Sass et al. 1971) and *in situ* (Beck et al. 1971). The bulk thermal conductivity of most sedimentary rocks ranges between 1.5 $Wm^{-1}K^{-1}$ (shales) and 4.5 $Wm^{-1}K^{-1}$ (sandstones) (Table 9.2). These estimates depend mostly on the mineralogy of the framework grains, the type and amount of material in the matrix (commonly clay minerals), and the porosity and fluid content (commonly water) (Brigaud and Vasseur 1989). The individual conductivities of framework, matrix, and pore-fluid are also dependent on temperature. The general trend is that nonargillaceous rocks have higher conductivities than argillaceous rocks, and that conductivity increases with increasing porosity. If measurements of the thermal conductivities of the different components in a rock can be made, the bulk thermal conductivity of the sedimentary layer can be estimated. The overall thermal conductivity structure of the basin-fill can then be estimated from a knowledge of the mineralogy, porosity, and fluid content of the stratigraphy filling the basin. The availability of large "continuous" subsurface datasets from hydrocarbon exploration boreholes has revolutionized the ability to make such estimates.

The *effective thermal conductivity* of a clean quartzose sandstone with pore-filling water should decrease with increasing porosity, since the pore fluid is insulating. However, the effective thermal conductivity of a clean quartzose sandstone with depth may be almost invariant (Fig. 9.13b). This is because of the decrease in conductivity of the framework quartz grains with increasing temperature, which offsets the increase in conductivity due to compaction (porosity loss) (Palciauskas 1986).

The effects of clays in a sandstone, for example as pore-filling authigenic cements, is to decrease the bulk thermal conductivity of the argillaceous sandstone, since clays have an insulating effect (Fig. 9.13a). Felspar and most clays do not show a marked effect of temperature on thermal conductivity, so the effect of compaction commonly dominates. A clay–water mixture (shales) increases in conductivity rapidly with depth because of compaction (§9.2), whereas a feldspar–water mixture, because it compacts similarly to a sand, increases in conductivity much more slowly with depth (Fig. 9.13c).

The bulk conductivity of a sediment layer can therefore be thought of as being made up of the contributions of the pore-fluid and the grain conductivities. Assuming a geometric mean model for the two-phase media of solid and fluid (Woodside and Messmer 1961), the bulk conductivity is

$$K_{bulk} = K_s^{(1-\phi)} K_w^{\phi} \quad (9.46)$$

where K_s and K_w are the thermal conductivities of sediment grains and water respectively and ϕ is the porosity, assumed to be filled with water. An alternative method, termed the *effective medium* theory calculates an effective bulk thermal conductivity for a randomly inhomogeneous medium made of constituents with volume fractions V_i and thermal conductivities K_i. The basic result of the theory is

Table 9.2 Density and thermal properties of some common minerals and rock types.

Rock type	Density ($kg\,m^{-3}$)	Thermal conductivity K^* ($Wm^{-1}K^{-1}$)	Volumetric coefficient of thermal expansion α_v ($10^{-5}K^{-1}$)
Minerals common in sediments and sedimentary rocks			
Water (pore-fluid)	1000	0.6	–
Quartz	2650	7.7	–
Calcite	2710	3.3	–
Dolomite	2870	5.3	–
Anhydrite	2960	6.3	–
Kaolinite	2630	2.6	–
Chlorite	2780	3.3	–
Illite/smectite	2660	1.9	–
Sedimentary rocks			
Shale	2100–2700	1.2–3.0	–
Sandstone	1900–2500	1.5–4.2	3
Limestone	1600–2700	2.0–3.4	2.4
Dolomite	2700–2850	3.2–3.5	–
Metamorphic			
Gneiss	2600–2850	2.1–4.2	–
Amphibolite	2800–3150	2.1–3.8	–
Igneous			
Basalt	2950	1.3–2.9	–
Granite	2650	2.4–3.8	2.4
Gabbro	2950	1.9–4.0	1.6
Peridotite	3250	3.0–4.5	2.4

Note:
* Thermal conductivities at surface temperatures (in part from Brigaud and Vasseur 1989).

$$K^{-1} = \sum_{i=1}^{n} 3V_i(2K + K_i)^{-1} \tag{9.47}$$

This expression is particularly useful where mixed components are present in the sediment layer. For example, for the water–quartz mixture mentioned above, if the quartz framework ($K_q = 5.4\ Wm^{-1}°C^{-1}$ at $T = 100°C$) occupies 0.7 of the rock volume and water ($K_w = 0.7\,W\,m^{-1}°C^{-1}$ at $T = 100°C$) occupies 0.3 of the rock volume, the bulk conductivity from effective medium theory (9.47) is approximately $3.3\,Wm^{-1}°C^{-1}$. From the general result in (9.46), the bulk conductivity is approximately $2.9\,Wm^{-1}°C^{-1}$.

A fundamental result of maintaining a constant heat flux through a heterogeneous basin fill is that the geothermal gradient must vary with depth. As an example, consider the thermal conductivity structure derived from the borehole shown in Figure 9.14a. Keeping the basal heat flux at $63\,mW\,m^{-2}$, the geotherm varies as in Figure 9.14b. Clearly, the presence of a heterogeneous basin-fill negates the assumption of a linear conduction geotherm. The implications for the interpretation of maturity profiles are discussed in §9.8.

9.6.2 Effects of internal heat generation in sediments

Heat generation by radioactive decay in sediments may significantly affect the heat flow in sedimentary basins (Rybach 1986). Although all naturally occurring radioactive isotopes generate heat, the only significant contributions come from the decay series of uranium and thorium and from ^{40}K (Table 9.3). As a result, heat

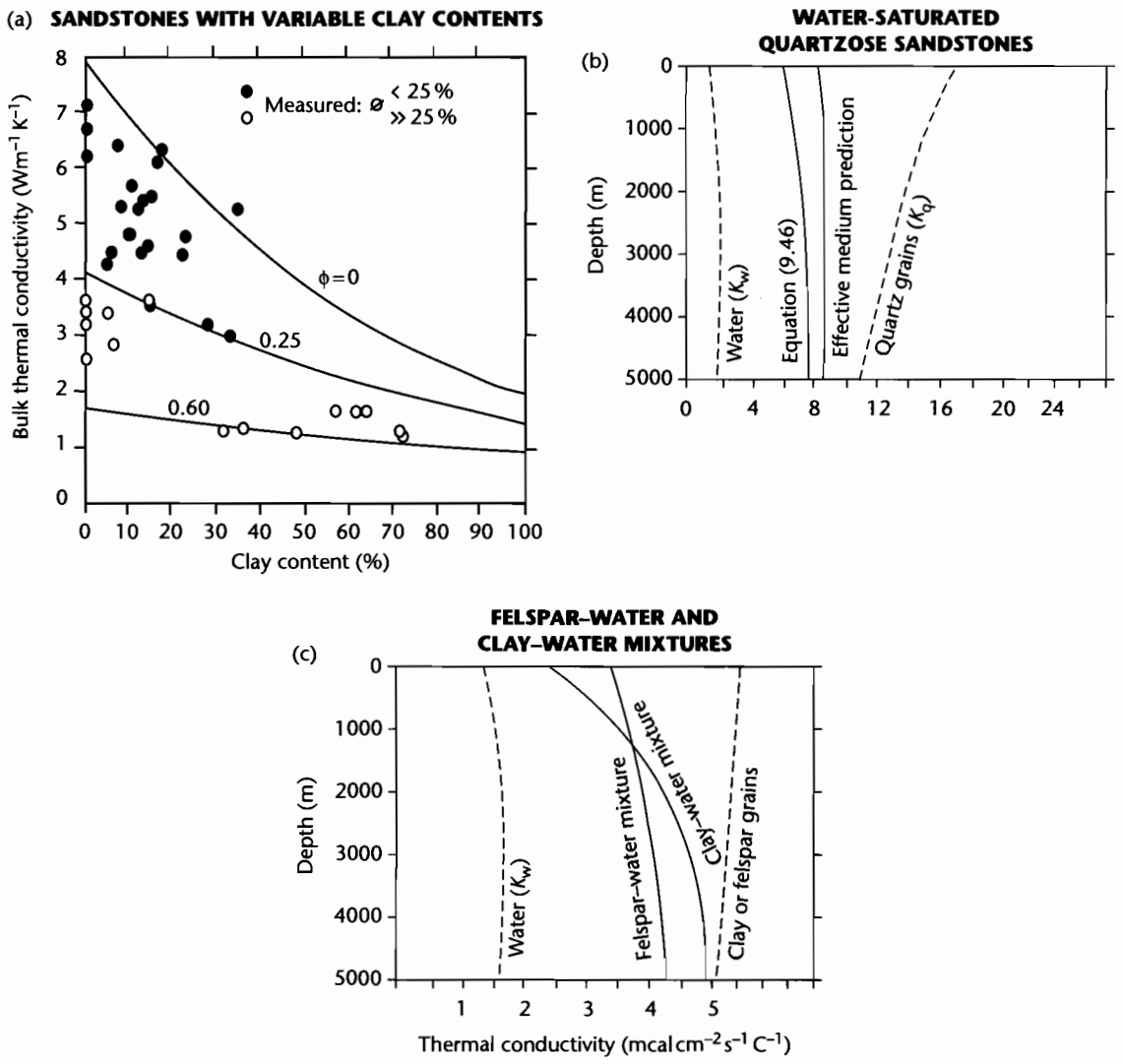

Fig. 9.13 The thermal conductivities of sedimentary rocks. (a) Influence of mineralogy on thermal conductivity of water saturated sandstones with a variable clay content, using thermal conductivities of $7.7\,W\,m^{-1}\,K^{-1}$, $2.0\,W\,m^{-1}\,K^{-1}$, and $0.6\,W\,m^{-1}\,K^{-1}$ for quartz, clay, and water respectively (after Brigaud and Vasseur 1989); (b) Thermal conductivity of water-saturated quartzose sandstone as a function of depth. The effective medium prediction and the empirical relation closely agree, demonstrating a negligible increase in thermal conductivity with depth, despite the fact that the quartz grains decrease in thermal conductivity considerably with depth; (c) Felspar–water and clay–water mixtures, showing that the thermal conductivities increase markedly with depth, especially for clay-rich sediments. This is principally due to the effects of compaction. In (b) and (c) the temperature gradient is $30\,°C\,km^{-1}$ and the surface temperature 20 °C. After Palciauskas (1986).

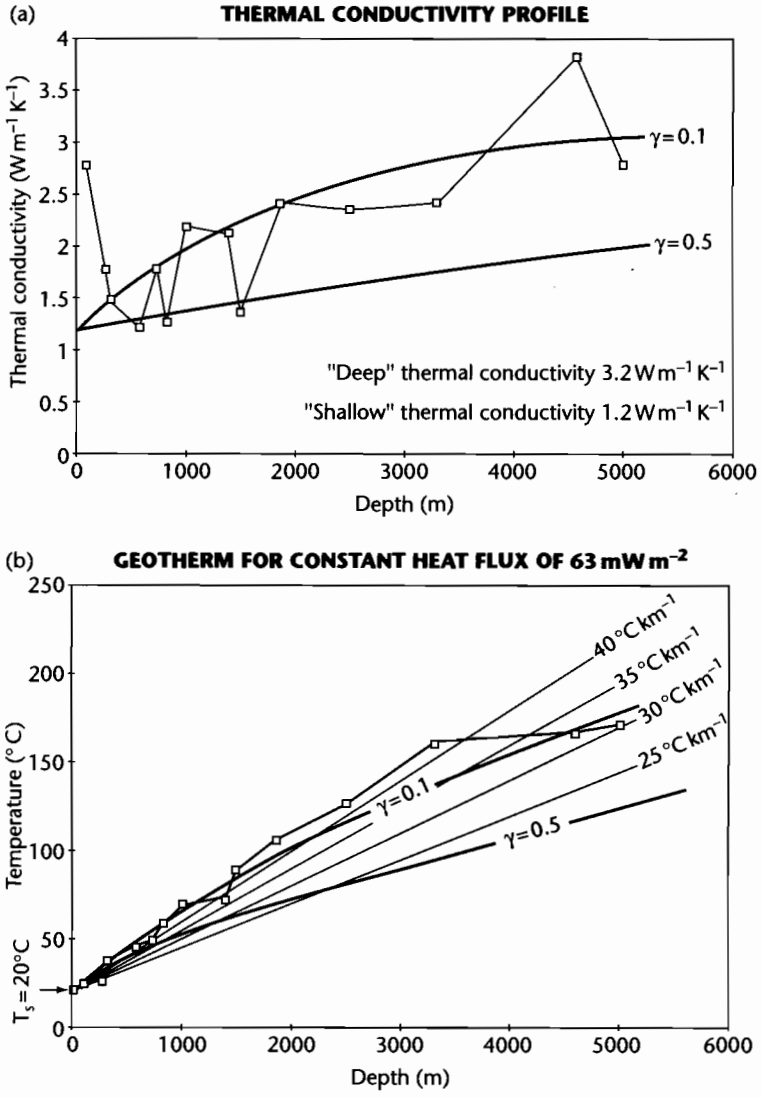

Fig. 9.14 (a) Thermal conductivity structure of stratigraphy penetrated by borehole 14/20-1 close to Wexford, southeastern Ireland. Two curves represent exponential distribution of thermal conductivity with depth with a depth constant γ of 0.1 and 0.5. The thermal conductivity in the deep section is *c.* 3.2 W m^{-1} K^{-1}, and *c.* 1.2 W m^{-1} K^{-1} in the shallow, near-surface section; (b) Geotherm using the thermal conductivity structure in (a) and a constant basal heat flow of 63 mW m^{-2}. Linear geotherms between 25 and 40 °C km^{-1} are shown for comparison.

production varies with lithology, generally being lowest in evaporites and carbonates, low to medium in sandstones, higher in shales and siltstones and very high in black shales (Haack 1982; Rybach and Cermak 1982; Rybach 1986).

In the continents, crustal radioactivity may account for a large proportion (20–60%) of the surface heat flow (Chapter 2). For a purely conductive, 1-D (vertical) heat flow, the temperature at any depth y is determined by the surface temperature T_0, the basal heat flow q_b, the

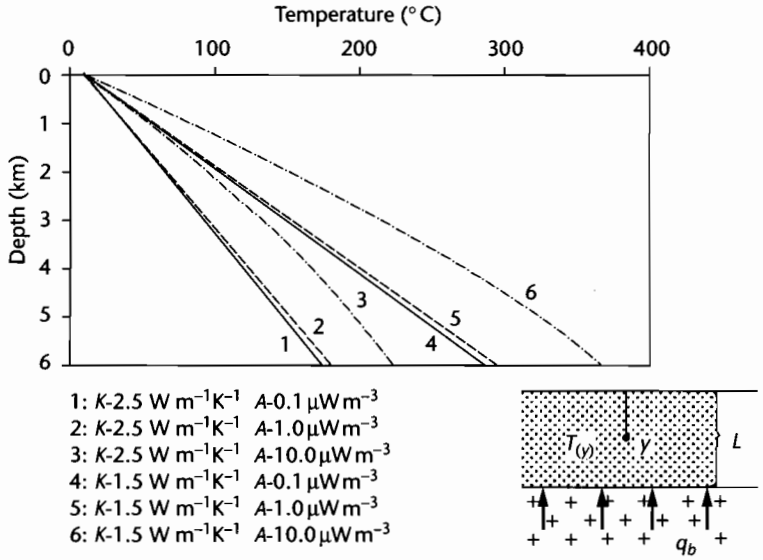

Fig. 9.15 The influence of internal heat generation per unit volume in the sedimentary column A and the thermal conductivity K on the distribution of temperature with depth $T(y)$. The different curves were calculated by Rybach (1986) for a thickness of the heat-producing zone of 6 km, a basal heat flux q_b of 70 mW m^{-2} and a surface temperature T_0 of 20 °C.

Table 9.3 Typical concentrations of heat-producing elements in various rock types.

Rock type	U (ppm)	Th (ppm)	K (%)
Granite	4.7	20	4.2
Shale	3.7	12	2.7
Average continental crust	1.42	3.6	1.43
Reference mantle	0.031	0.124	0.031
Chondritic meteorite	0.008	0.029	0.056

average thermal conductivity of the sediments K and the internal heat production A (estimated from natural gamma ray logs) (eqn 2.46). The effect of the internal heat generation is greatest at large depths, as can be seen from the third term in equation (2.46) (Fig. 9.15). The temperature increase after a time t as a result of the internal heat generation depends on the value of A, but the net temperature change also depends on the rate of conductive heat loss. Over geological time scales of >10 Myr the temperature rise may be considerable (Rybach 1986, p.317). Internal heat generation in sediments may therefore strongly affect the temperature field in the basin if it is deep (>5 km) or long-lived (>10 Myr).

The presence of a thick cover of sedimentary rocks with high radiogenic heat production has the effect of "blanketing" the underlying crust and deeper parts of the sedimentary basin (Karner 1991; Wangen 1995). This blanketing effect may be important in terms of the temperature-dependent rheology of rocks underlying the basin, but more importantly in the present context in elevating paleotemperatures in the basin-fill.

9.6.3 Effects of water flow

The temperatures in sedimentary basins may also be affected by the advective flow of heat through regional aquifers. Such processes may cause anomalously low surface heat flows at regions of recharge, and anomalously high surface heat flows in regions of discharge. The heat flow distributions of the Great Plains, USA (Gosnold and Fischer 1986) and the Alberta Basin (Majorowicz and Jessop 1981; Majorowicz et al. 1984) have been explained in this way.

It is important to know the relative contributions of conduction from the interior of the Earth, internal heat production from radiogenic deacy (and chemical reactions), and advective transport of fluids through pore space. We perform this heat balance in Boxed Text 9.3

BOXED TEXT 9.3: Advective Heat Transport by Fluids

Consider a subsiding and compacting volume of porous rock with a cross-sectional area a and thickness δy (Fig. 9.16). The total heat gain or loss across this volume of porous rock of thickness δy is made of three components: a change in conductive heat flow q_c, an internal heat generation A, and a change in advective heat flow q_a

$$(a\partial y)\frac{\partial q_c}{\partial y}+(a\partial y)A+(a\partial y)\frac{\partial q_a}{\partial y} \tag{9.48}$$

The mass of the rock volume is $\rho_r a\delta y$ where ρ_r is the density of the porous rock. The heat stored in this rock volume is therefore the product of the specific heat c_r and its mass, $c_r\rho_r a\delta y$. If this rock volume undergoes a temperature change δT over a short time period δt, the rate of heat loss or gain is $c_r\rho_r a\delta y\delta T/\delta t$. Consequently,

$$c_r\rho_r a\partial y\frac{\partial T}{\partial t}=(a\partial y)\frac{\partial q_c}{\partial y}+(a\partial y)A+(a\partial y)\frac{\partial q_a}{\partial y} \tag{9.49}$$

The mass of fluid occupying the pore space is $(a\delta y\rho_f\phi)$. Its heat content is therefore $(a\delta y\rho_f\phi)c_f T$, and the advective heat flow is

$$q_a=(a\partial y)\rho_f\phi c_f v_f T \tag{9.50}$$

Substituting (9.50) into (9.49), making use of Fourier's law (eqn 2.29), simplifying and rearranging, equation (9.49) can be written

$$\frac{\partial T}{\partial t}=\frac{1}{c_r\rho_r}\left\{K_r\frac{\partial^2 T}{\partial y^2}+A+c_f\rho_f\phi v_f\frac{\partial T}{\partial y}\right\} \tag{9.51}$$

where K_r is the thermal conductivity of the rock volume, and it is assumed that the pore fluid velocity v_f does not vary with depth in the rock volume.

Clearly, one of the most important parameters in an analysis of the temperature changes caused by advection of pore waters is the flow velocity of the moving groundwater. Flow velocities of groundwater vary greatly, from very high velocities in shallow unconfined aquifers (>10^3 m yr^{-1}, equivalent to *c.* >10^{-4} m s^{-1}), lower values in common producing aquifers (10^{-1} to 10^2 m yr^{-1}, equivalent to *c.* >10^{-5} to 10^{-8} m s^{-1}), and very low velocities of compactionally driven flow (10^{-6} to 10^{-2} m yr^{-1}, equivalent to *c.* >10^{-13} to 10^{-9} m s^{-1}) (Fig. 9.17). Using the parameter values for a volume of rock deeply buried in a sedimentary basin (Table 9.4)

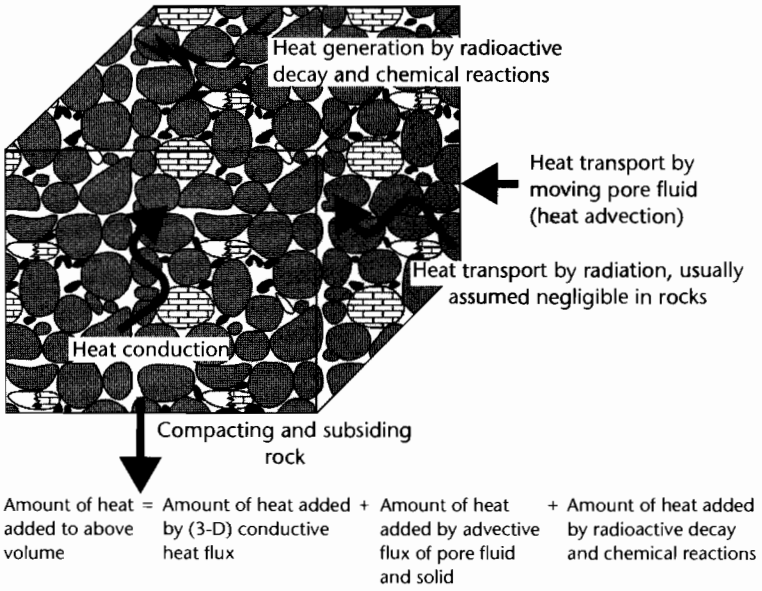

Fig. 9.16 Schematic representation of a cube of subsiding and compacting sedimentary rock as a basis for a heat balance (after Giles 1997). Reproduced courtesy of Springer.

Table 9.4 Typical parameter values for a porous sedimentary unit deeply buried in a sedimentary basin.

Parameter	Notation	Typical value	Units
Rock volume density	ρ_r	2500	$kg\,m^{-3}$
Rock volume bulk thermal conductivity	K_r	3	$Wm^{-1}K^{-1}$
Rock volume heat capacity	c_r	1×10^3	$J\,kg^{-1}K^{-1}$
Pore fluid density	ρ_f	1000	$kg\,m^{-3}$
Pore fluid heat capacity	c_f	4.185×10^3	$J\,kg^{-1}K^{-1}$
Pore fluid velocity*	v_f	10^{-13}–10^{-9}	$m\,s^{-1}$
Rock volume porosity	ϕ	0.1	
Internal heat generation	A	1.25×10^{-6}	Wm^{-3}
Formation and pore fluid temperature	T	373	K

Note:
* Typical of compactionally driven flow (see Giles 1997, p. 278, Fig. 12.3).

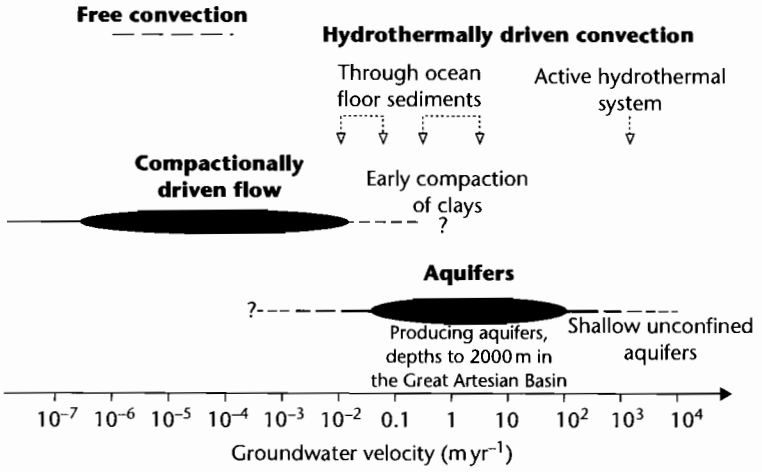

Fig. 9.17 Typical measured pore fluid velocities associated with compactionally driven flow, confined and unconfined aquifers and hydrothermally driven convection, after Giles (1997). Reproduced courtesy of Springer.

equation (9.50) gives an advective heat flow of 16 mW m^{-2} for a pore fluid velocity of 10^{-10} m s^{-1} and 2 mW m^{-2} for a pore fluid velocity of 10^{-11} m s^{-1}, typical of compaction-driven flow (Giles 1997, p. 278). Advective heat flows are therefore likely to be important in porous sedimentary rocks (such as uncemented eolian sandstones) with compaction-driven groundwater velocities, and to dominate in aquifers with high groundwater velocities (10^{-6} to 10^{-7} m s^{-1}).

Flow velocity can be estimated from the *Darcy equation*

$$U = K\frac{\partial P}{\partial x} \tag{9.52}$$

where K is the permeability and $\delta P/\delta x$ is the pressure gradient. Flow velocities are therefore strongly dependent on lithology. With compaction during burial, sedimentary units become less permeable and therefore less able to transmit fluids.

and, taking reasonable parameter values for a deeply buried rock in a sedimentary basin, calculate the role of advection in controlling the heat flow.

The likely impact of fluids on the thermal history of the basin-fill is linked to the tectonic evolution of the basin. For example, uplift of rift shoulders during stretching of the continental lithosphere may cause meteoric-derived groundwater flows driven by the topographic elevation of the basin flanks. The meteoric fluxes in this case must displace brines filling pore space within the basin-fill. If the density of pore-filling brine is $1028\,kg\,m^{-3}$ and the density of meteoric water is $1000\,kg\,m^{-2}$, a simple pressure balance indicates that the extent of downward penetration of meteoric water is nearly 40 times the topographic elevation of its influx (Bjorlykke 1983). This implies that for even low topographic basin margin uplifts, meteoric gravitationally driven water is able to displace basinal brines from the entire depth of the sedimentary basin. At the other extreme, fluid movement caused by progressive compaction of basin sediments is slow, with vertical rates of $<10\,mm\,yr^{-1}$, with lower values still as the permeability reduces during compaction (Giles 1987) (Fig. 9.17).

Smith and Chapman (1983) provide a review of the effects of fluid flow on heat flow in regional scale systems. Luheshi and Jackson (1986) have applied the theory of Smith and Chapman (1983) to the Alberta Basin. Using a permeability and thermal conductivity structure for the basin, they were able to explain the raised temperatures at discharge points of fluid flow and lowered temperatures at the recharge areas in the fringing hills (Fig. 9.18). The model results suggest that the temperature distribution is dominated by convection above the Paleozoic succession, while the heat flows within the Precambrian section can be explained simply by conduction. Andrews-Speed et al. (1984) similarly found that heat flow measurements strongly suggested a deep water circulation, possible controlled by the configuration of faults, in the North Sea failed rift. The implications of detailed studies such as this are that simple 1-D conductive heat flow models may be very poor predictors of actual heat flows in some sedimentary basins. The most strongly affected basins are likely to be continental basins with marginal uplifts, such as foreland basins and some intracratonic rifts and sags.

9.6.4 Effects of surface temperature changes

The possible effects of surface temperature changes on the maturation of thermal indicators have been relatively neglected, although the effects of, for example, glacial retreat on near-surface temperatures has been evaluated (Beck 1977). The likelihood of a surface temperature change penetrating an underlying basin-fill is essentially a question of heat diffusion (§2.2.4), and the problem can therefore be approached in a similar way to the cooling of the oceanic lithosphere. The amount of time necessary for a temperature change to propagate a distance l in a medium with thermal diffusivity κ is

$$\tau = \frac{l^2}{\kappa} \tag{9.53}$$

and the characteristic distance (or thermal diffusion distance) over which a temperature change is felt is

$$L = \sqrt{\kappa t} \tag{9.54}$$

Taking a thermal diffusivity of $\kappa = 10^{-6}\,m^2\,s^{-1}$, appropriate for the sandstones of a basin-fill, a surface temperature disturbance would be registered at 1 km depth in just over 30 kyr. Expressed differently, the surface temperature change would propagate to a depth of 5.6 km in 1 Myr. We should therefore expect a surface temperature change to rapidly propagate through the upper part of the basin-fill. O'Sullivan and Brown (1998) for example, suggested that the effects of a surface temperature change of *c.* 17 °C during the Miocene on the North Slope of Alaska could be recognized in apatite fission tracks in borehole samples. If geotherms derived from apatite fission track analysis were used to calculate denudation in this example, estimates would be significantly in error.

A key point in this argument is that for thermal indicators to be affected by a surface temperature change, the surface temperature change must be sustained for a prolonged period of time. Yet, climatically induced surface temperature changes tend to be cyclic. What would be the effect of a periodic variation in surface temperature on the geotherm? Temperatures must vary cyclically within a surface zone of the Earth whose thickness is determined by the thermal properties of the crust or basin-fill and the period of the temperature fluctuation. If the temperature variation is described by

$$\omega = \frac{2\pi}{f} \tag{9.55}$$

where f is the period of the temperature variation, we can define a *skin depth* L at which the amplitude of the temperature variation is 1/e of that at the surface of the Earth

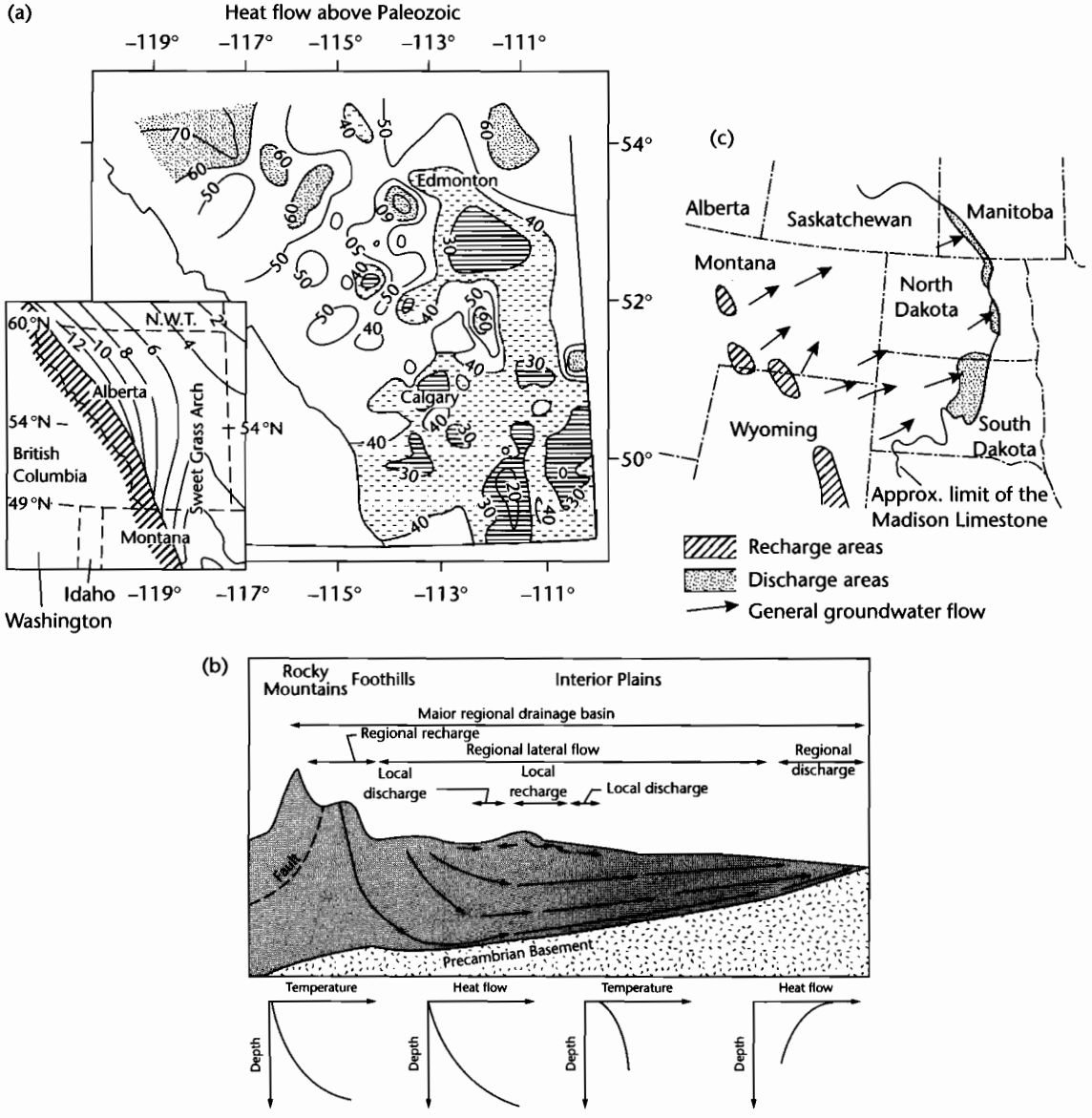

Fig. 9.18 Effects of groundwater flow on surface heat flows in sedimentary basins. (a) Heat flow map of southern and central Alberta, Canada based on estimated heat flow values (in $mW m^{-2}$) above the top of the Paleozoic, based on 33,653 bottom hole temperature data from 18,711 wells (Majorowicz et al. 1984). The heat flows are strongly influenced by groundwater flow from recharge areas in structurally high regions, such as the Sweet Grass Arch (inset), to discharge areas; (b) Pattern of recharge and discharge in a cross-section from the Rocky Mountains to the Great Plains (after Majorowicz et al. 1984), and (c) plan view of groundwater flow in the Mississippian (Lower Carboniferous) Madison Limestone aquifer (after Downey 1984).

$$L = \sqrt{\frac{2\kappa}{\omega}} \tag{9.56}$$

Using $\kappa = 8 \times 10^{-6}\,m^2 s^{-1}$, it is clear that the skin depth for daily temperature variations ($\omega = 7.27 \times 10^{-5}\,s^{-1}$) is less than 20 cm, but for Pleistocene climate change variations of frequency 10^5 yr ($\omega = 1.99 \times 10^{-12}\,s^{-1}$), the skin depth is 1 km. This means that long period variations in surface temperature may be felt deep within the sedimentary basin-fill.

9.7 MEASUREMENTS OF THERMAL MATURITY IN SEDIMENTARY BASINS

Approaches to understanding the mechanisms of subsidence and uplift in sedimentary basins invariably involve model predictions for burial history, heat flow, and paleotemperature that can be compared with reality. But what direct observations are possible in a sedimentary basin that provide information on thermal history and thereby allow a test and calibration of these models? A wide range of techniques are currently available, making use of the changes with temperature of organic particles, clay minerals, geochemical markers, and of the annealing and diffusion histories of certain minerals such as apatite. Most of these techniques generate data on the *maximum* temperature reached by a particle within the basin-fill. This is because thermal reactions are irreversible. Only thermochronological techniques such as apatite fission track analysis and U–Th/He diffusion analysis provide any information on thermal evolution. Each technique has its advantages and drawbacks. Taken together, a range of diverse techniques may provide important information on the thermal history of the basin-fill. This information is critically important not only in understanding the driving mechanisms for basin formation, but also in the evaluation of hydrocarbon prospectivity (Tissot and Welte 1978) (Chapter 10).

In the following sections, a number of techniques are presented in outline. For further information and detailed applications, the reader is referred to the references cited. Useful summaries are found in Héroux et al. (1979), Gallagher et al. (1998) and Giles (1997).

9.7.1 Estimation of formation temperature from borehole measurements

Formation temperatures from boreholes are used in thermal modeling studies to calculate the geothermal gradient and basal heat flow to the sedimentary section. The temperature in the borehole is recorded on each logging run, using a suite of maximum recording thermometers. Because the circulation of drilling fluid tends to cool the formation, it is necessary to analyze the rate at which temperature restores itself to its original true formation value using temperatures recorded on each successive logging run within a suite of logs. These temperatures may be plotted on a "Horner"-type plot, as described by Dowdle and Cobb (1975).

The form of the temperature build-up plot is shown in an example from the Gulf Coast in Figure 9.19. Temperature measured on each logging run is plotted against

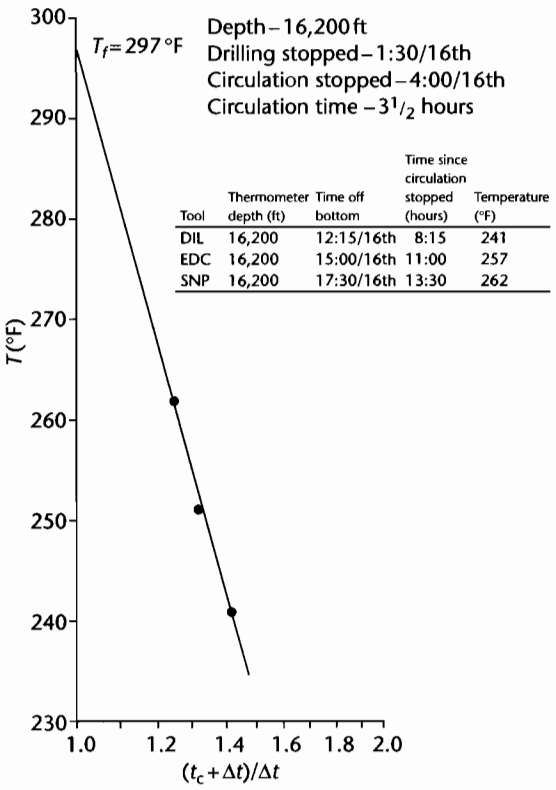

Fig. 9.19 The determination of true formation temperature from a Horner plot (after Dowdle and Cobb 1975). This example is from a high temperature well in the Gulf Coast, USA. The depth at which measurements were taken was 16,200 ft (*c.* 5 km). Temperature increased from 241 °F measured at 8 h 15 min after circulation of mud stopped, to 262 °F taken 13 h 30 min after circulation stopped. The estimated formation temperature T_f is 297 °F.

a dimensionless time factor, $(t_c + \Delta t)/\Delta t$, where t_c is the cooling time (the duration of mud circulation from the time the formation opposite the thermometer was drilled to the time circulation of the drilling mud stopped), Δt is the thermal recovery time (time since mud circulation stopped to the time the logging sonde is in position at the bottom of the borehole). A fully recovered or stabilized formation temperature T_f is obtained by extrapolation to the ordinate, where $(t_c + \Delta t)/\Delta t = 1$. Serra (1984, 1986) discusses the calculation of heat flow from borehole temperature measurements.

9.7.2 Organic indicators

The progressive maturation of organic materials has long been understood in terms of *coal rank*. The coalification process changes peat to anthracite through the intermediate steps of brown coal (lignite and sub-bituminous coal) and bituminous coal. During coalification, the percentage of carbon increases whereas moisture and volatiles are gradually eliminated (Fig. 9.20). Of much greater importance to basin analysis is the quantitative measurement of maturity through the reflectance of the vitrinite maceral, and to a lesser extent the structural changes in distinctive organic molecules known as biomarkers, and the semi-quantitative assessment of spore color.

9.7.2.1 Vitrinite reflectance

Vitrinite reflectance is the most widely used indicator of maturity of organic materials. It is an optical parameter and is denoted by VR or R_o (reflectance in oil). Standard procedures for the measurement of vitrinite reflectance are given in Bostick and Alpern (1977), Bostick (1979), Hunt (1979), Dow and O'Connor (1982), Stach et al. (1982), van Gijzel (1982), and Tissot and Welte (1984). Section 10.3.1.3 provides more details. The reflectance of the vitrinite group of macerals appears to vary smoothly and predictably with temperature (Lopatin 1971; Burnham and Sweeney 1989; Sweeney and Burnham 1990).

Drawbacks in the use of vitrinite reflectance measurements are outlined by Héroux et al. (1979), Kübler et al. (1979) and Durand et al. (1986). These arise from a number of problems. Reflectance measurements taken from maceral types other than vitrinite (especially in lacustrine and marine sediments), and even from different macerals within the vitrinite group, may significantly differ (Bensley and Crelling 1994). Other drawbacks are the possibility of reworking of organic material (especially in sandstones), and the lack of higher plants yielding vitrinite in pre-Devonian strata. Vitrinite reflectance tends to be unreliable at low levels of thermal maturity (R_o less than 0.7 or 0.8%). At high temperatures equivalent to depths of >4 km the vitrinite maceral is increasingly anisostropic, making accurate measurement problematical. Nevertheless, with care, reflectance values are a good indicator of maximum paleotemperature within the approximate depth range of 1–4 km (Whelan and Thompson-Rizer 1993).

Unfortunately, the distribution of activation energies and value of the frequency factor (see eqn 9.40) for the maturation of vitrinite are not convincingly known (Lerche et al. 1984; Burnham and Sweeney 1989; Lakshmanan et al. 1991), and a wide range of values have been proposed. The most reliable estimates give a value of E_a in the range 200–300 kJ mol^{-1}, and of A from 2.5×10^{10} to 7.48×10^{18} s^{-1}. It must be emphasized therefore that the uncertainties in knowledge of the parameters in the Arrhenius equation make the use of vitrinite reflectance data useful but inexact, and VR measurements should always be compared with paleotemperature estimates from other indices.

Vitrinite reflectance measurements from samples recovered at different depths allows a plot of vitrinite reflectance *versus* depth to be made (e.g., Corcoran and Clayton 2001). These plots are known as VR or R_o profiles. Examples of their interpretation are given in §9.8. A compilation of VR data from 28 extensional basins shows a relatively well-defined trend (Fig. 9.21), with a surface intercept at 0.2–0.4% R_o, and a gradient of $0.15 \pm 0.09\%$ R_o km^{-1} at depths of <4 km.

The Anadarko Basin in western Oklahoma has some of the deepest exploratory wells in the world, penetrating to more than 7900 m (~26,000 ft), and is therefore an excellent case study for thermal maturation. Vitrinite reflectance contours (*isoreflectance lines*) on the Upper Devonian–Lower Mississippian *Woodford Shale* have been constructed from 28 boreholes (Fig. 9.22) (Cardott and Lambert 1985). Isoreflectance maps are useful in combination with structural contours, since cross-cutting relationships give an indication of local thermal anomalies superimposed on the burial-related maturation.

Since vitrinite reflectance in a nonreversible thermal indicator, it is important to know whether the distribution of vitrinite reflectance with depth in a sedimentary basin allows a geotherm at a particular time in basin history to be constructed. For example, is it possible that

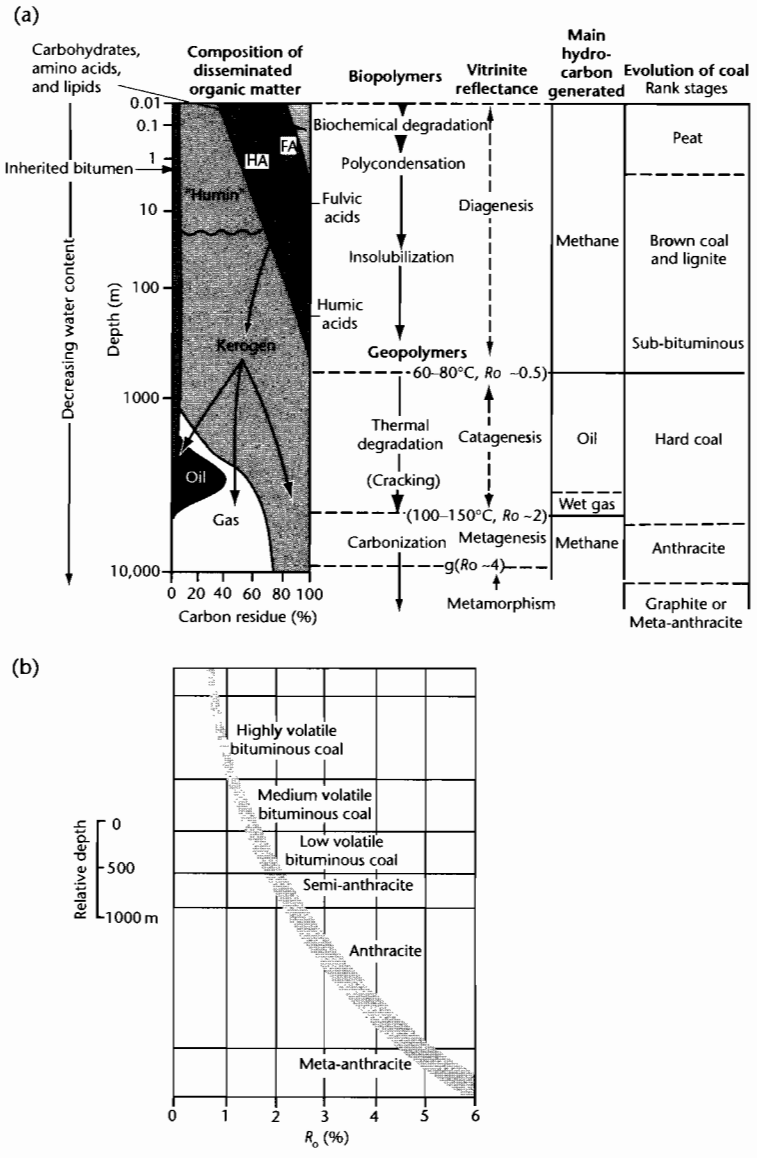

Fig. 9.20 (a) Evolution of organic matter from organic-rich sediment or peat through the various ranks of coal to meta-anthracite and the main hydrocarbons generated, correlated with vitrinite reflectance values. After Tissot and Welte (1984). Coal ranks from Stach et al. (1982). Reproduced courtesy of Springer; (b) Correlation of coal rank with vitrinite reflectance R_0 (%). Reproduced courtesy of Gebrüder Borntträger, Berlin.

the maximum temperature at different depths in the basin was reached at different times? If so, a R_o profile would not represent a single geotherm. This problem can be approached from a forward model of paleotemperature and vitrinite reflectance in a basin with a time-dependent basal heat flow. The heat flow and temperature algorithms are based on the uniform stretching model, but with an additional heat flow originating from the internal heat generation of crustal rocks and sediments due to radioactive decay. The time–temperature

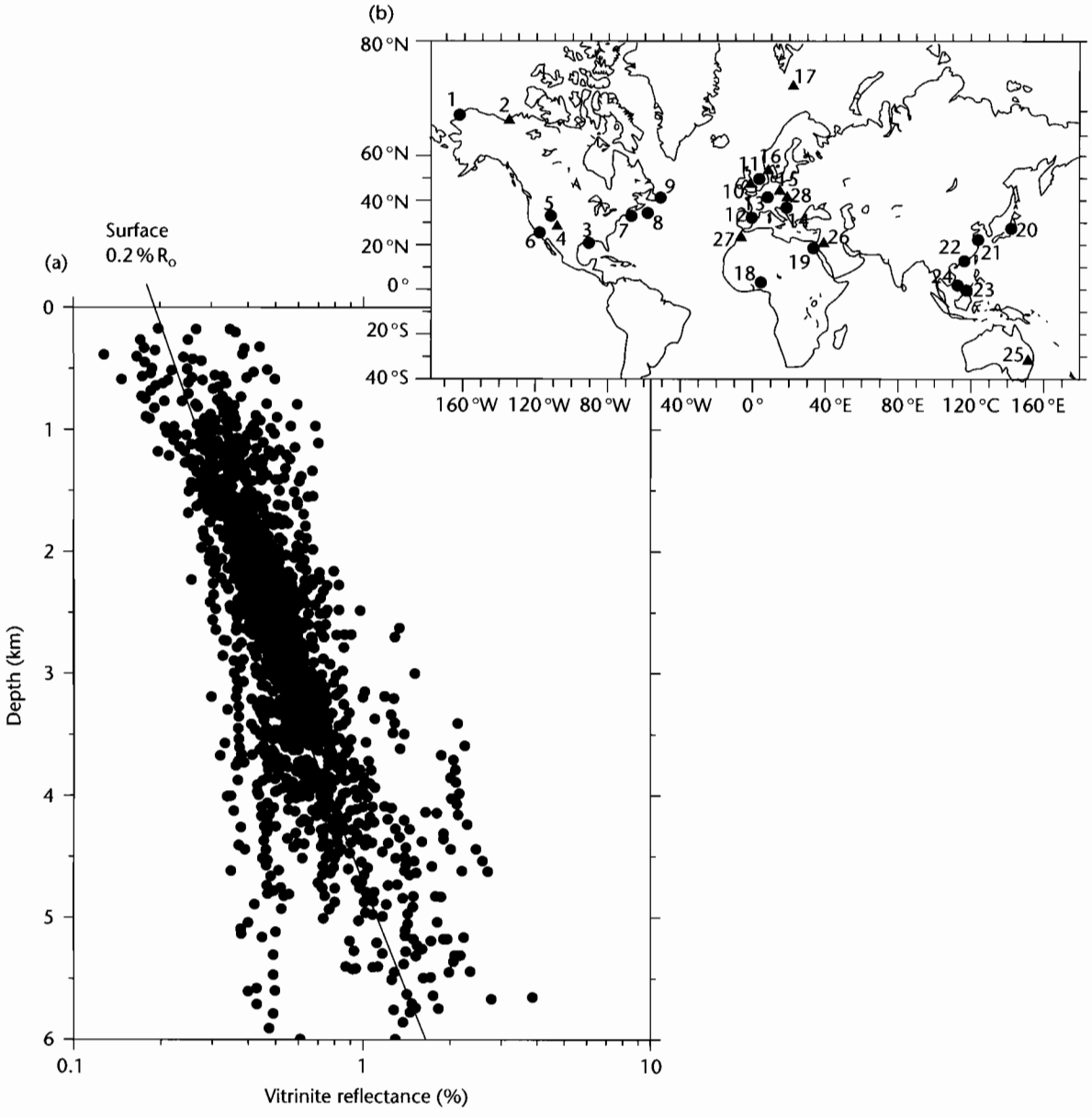

Fig. 9.21 Vitrinite reflectance (logarithmic scale) *versus* depth for a wide range of selected extensional sedimentary basins (marked on world map) with predictable subsidence histories, after Rowley and White (*pers. comm.*).

history of a number of horizons within a borehole can then be calculated based on the thermal model and the subsidence history derived from the stratigraphy penetrated by the borehole (see §9.3). Paleotemperatures can be converted to vitrinite reflectance using empirical relationships (Barker and Pawliewicz 1986; Burnham and Sweeney 1989; Sweeney and Burnham 1990) to create a synthetic VR profile. Two interacting effects control the paleotemperature and vitrinite reflectance of the basin-fill. On the one hand, the basal heat flux decreases

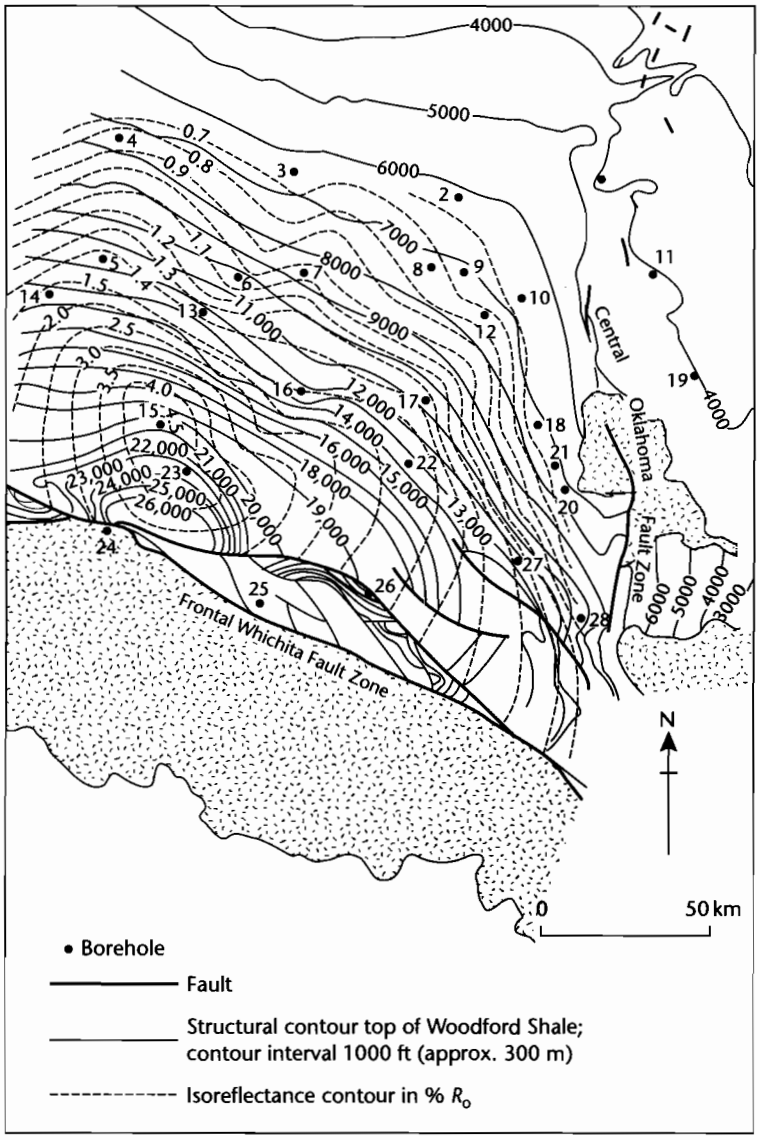

Fig. 9.22 Combined isoreflectance and structure map of the Woodford Shale of the Anardarko Basin of Oklahoma (Cardott and Lambert 1985). Vitrinite reflectance values in general increase with depth of burial, but strong cross-cutting relationships of the isoreflectance and structure contours suggest that there may have been local thermal disturbances superimposed on the burial-related maturation.

through time due to thermal relaxation following stretching, causing cooling. On the other hand, subsidence causes a reference horizon to descend to increasing depths over time, causing heating. Figure 9.23 shows that for low to moderate values of stretching in a basin undergoing continuous subsidence, the present-day temperatures represent the maximum temperatures reached by all but the deepest horizons within the basin-fill. Consequently, the vitrinite reflectance profile can be used to estimate the geotherm. However, model results suggest

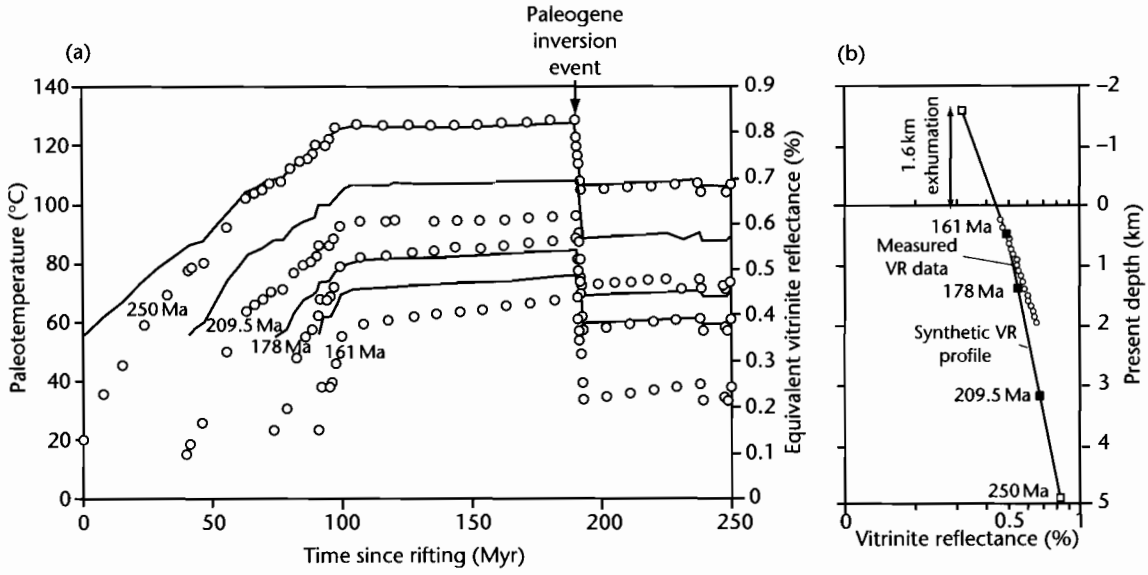

Fig. 9.23 (a) Paleotemperature and equivalent vitrinite reflectance *versus* time for 4 different horizons in well 42/21-1 in the extensional Irish Sea Basin ($\beta = 1.5$ at 250 Ma) with internal heat generation ($H_s = 9.6 \times 10^{-10}$ W kg^{-1}; $h_r = 10$ km) and the thermal conductivity structure shown in Fig. 9.14. Open circles are data points derived by forward modeling temperature from the borehole subsidence history. Solid lines are equivalent vitrinite reflectance; (b) The forward modeled R_0 profile is compared with measured values. Extrapolation of the profile upwards gives an estimate of 1.6 km of denudation since the VR values were set at the maximum temperature at *c.* 60 Ma (*c.* 190 Myr since rifting).

that in highly stretched basins and for old (especially synrift) stratigraphy, VR values may represent maximum paleotemperatures attained early in basin history and not subsequently exceeded. Consequently, measured VR profiles may not reflect closely the distribution of temperature with depth at any particular instant in time.

The use of R_o profiles in estimating the amount of section removed as a result of basin inversion events is discussed in §9.8.2.

Although vitrinite reflectance has become pre-eminent in its use in basin studies, it is not the only index of thermal maturity (§10.3.1.3). Other optical parameters derived from organic material include sporinite microspectrofluorescence and spore, pollen, and conodont coloration scales. Fluorescence and reflectance studies are complementary, fluorescence intensity and reflectance being inversely proportional.

9.7.2.2 Biomarkers

Certain organic molecules (*biomarkers*) undergo transformations with increasing temperature. For example, single *isomers* in biological material are progressively converted to mixtures of isomers with increasing temperature (Abbott et al. 1990). *Aromatization* reactions can also be used, such as the conversion on mono-aromatic to tri-aromatic steroids (Mackenzie and McKenzie 1983). Biomarker transformations take place at rates approximated by the Arrhenius equation.

9.7.3 Thermochronology: Apatite fission track analysis

Fission track analysis is a relatively modern (since the 1960s) thermochronological technique based on the atomic damage caused to minerals by their spontaneous decay, almost exclusively by the fission of ^{238}U. The fission of ^{238}U produces a trail of damage to the lattice known as a *fission track*. Fission tracks become visible when the crystal is chemically etched and viewed at high magnification.

It is safe to assume that statistically fission takes place at a constant rate. The concentration of the parent isotope ^{238}U in minerals such as apatite ($Ca_5(PO_4)_3(F,Cl,OH)$), zircon ($ZrSiO_4$) and sphene

($CaTiO(SiO_4)$) is high enough to produce plenty of tracks, but low enough so that the crystal is not completely criss-crossed by tracks, making measurement difficult.

A *fission track age* (Hurford and Carter 1991) can be determined in a similar way to other radiometric methods, that is, through knowledge of the relative abundance of the parent and daughter products. In the case of fission track dating, the abundance of the parent is the original number of ^{238}U atoms – this can be estimated by irradiating the sample in a nuclear reactor. The abundance of the daughter product is proportional to the number of spontaneous fission tracks per unit volume of the apatite crystal.

There are a number of ways in which fission tracks can be measured and analyzed. The most common is to measure the lengths of between 50 and 150 individual horizontal tracks that have been etched just below the surface of the polished section of the crystal. These are known as *confined tracks*. The data are normally shown as a histogram of track length with a mean and standard deviation. Importantly, fission tracks are metastable features that fade or *anneal*, which causes track lengths to shorten. Annealing is mostly controlled by temperature (and also time), so track length distributions reveal information about thermal history. The higher the temperature experienced by the apatite crystal, the greater the annealing.

Individual minerals have a closure temperature below which fission tracks are preserved. For *apatite*, the closure temperature is 110 °C ± 10 °C, but at geological time scales there is a range of temperature of at least 60 °C below the closure temperature where significant annealing takes place: this is termed the *Partial Annealing Zone* (PAZ). Some annealing may even take place at room temperature, but it is generally regarded as negligible at these temperatures. For *zircon*, the PAZ is between 200 and 350 °C, but the annealing behavior of zircon is not as well known as for apatite. Because of the different closure temperatures of apatite and zircon, apatite fission track analysis is particularly useful in thermal studies of the upper few km of the crust, whereas zircon fission track analysis is more informative for deeper levels of burial.

In summary, fission tracks are continuously formed at all temperatures, but are only preserved for geological time scales below the closure temperature. Their abundance therefore gives a fission track age. The track length distribution gives a record of the annealing history, which can be related to the time–temperature trajectory of the crystal.

The fission track ages and track length distributions for four different thermal histories are shown in Figure 9.24. These are illustrative of the way in which apatite fission tracks are sensitive to different tectonic histories.

- **Linear heating** produces a tightly clustered, unimodal, symmetrical histogram of track length with a short mean track length (MTL); all tracks experience the same maximum temperature; the fission track age bears no relation to any specific or thermal event. Linear heating is likely to take place during progressive subsidence in a sedimentary basin;
- **linear cooling** causes tracks to experience different maximum temperature, causing the track length histogram to be negatively skewed; the MTL is longer and the standard deviation larger than in the case for linear heating; once again the fission track age bears no relation to any specific thermal or tectonic event. Linear cooling may result from prolonged, slow basin inversion;
- **rapid cooling** causes most tracks to have been produced after the early cooling episode at temperatures below those of the PAZ; track lengths are long; the fission track age gives a good indication of the date of the cooling event. Rapid cooling may result from tectonic processes driving rapid exhumation, for example on a rift flank or in an orogenic belt;
- **heating–cooling** scenario; old tracks formed during the heating phase have a similar length with a short MTL; newer tracks experience different maximum temperatures during the cooling phase, causing the histogram to be bimodal, with a high standard deviation; the fission track age does not accurately reflect the onset of uplift. Heating–cooling is typical of basin development followed by inversion.

Apatite fission track analysis is routinely used in the quantification of denudation in a wide range of tectonic situations including convergent mountain belts, rift flanks, and passive margin escarpments (useful summary in Gallagher et al. 1998). The rate of cooling derived from fission track thermochonometry is very valuable in estimations of long term sediment effluxes from erosional hinterlands, and in the timing of distinct tectonic exhumation events. For example, the onset of rapid exhumation in the Central Alaska Range was dated as 6 Ma on the basis of the recognition of two distinct populations of fission tracks (Fitzgerald et al. 1995). Some highly annealed tracks formed during a period of slow cooling, whereas other relatively unannealed tracks formed during a rapid exhumation event.

AFT analysis has also been extensively applied to the thermal history of sedimentary basins (Naeser 1979).

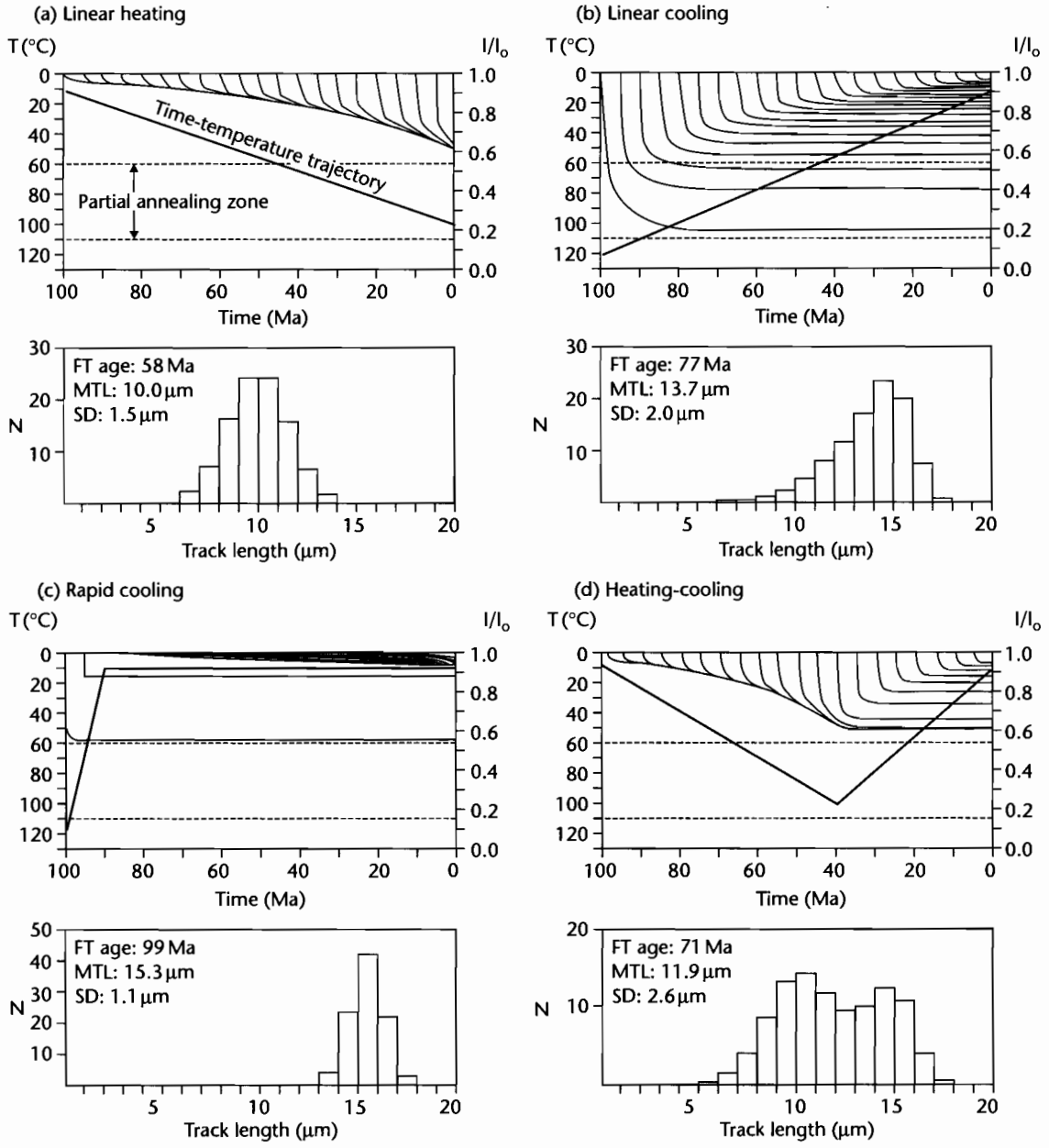

Fig. 9.24 Simple thermal histories and the predicted fission track length parameters using Durango apatite and the annealing model of Laslett et al. (1987), after Gallagher et al. (1998). Each model simulation has 20 tracks formed at equal time increments over the total duration of the thermal history. Track length reduction (annealing) is shown by the ratio l/l_0, where l is the track length and l_0 is the initial track length. (a) Linear heating, giving a symmetrical, unimodal track length distribution and a short mean track length. Note that the fission track age does not relate to any distinct tectonic or thermal event; (b) Linear cooling, with a negatively skewed track length distribution, since each track experiences a different maximum temperature. The fission track age does not correspond with any distinct tectonic or thermal event; (c) Rapid cooling, with long tracks caused by rapid exhumation through the Partial Annealing Zone. The fission track age gives a good indication of the age of the cooling event; (d) Heating–cooling trajectory gives a bimodal track length distribution, and the fission track age does not correspond to any distinct tectonic or thermal event. Reproduced courtesy of Annual Reviews, Palo Alto.

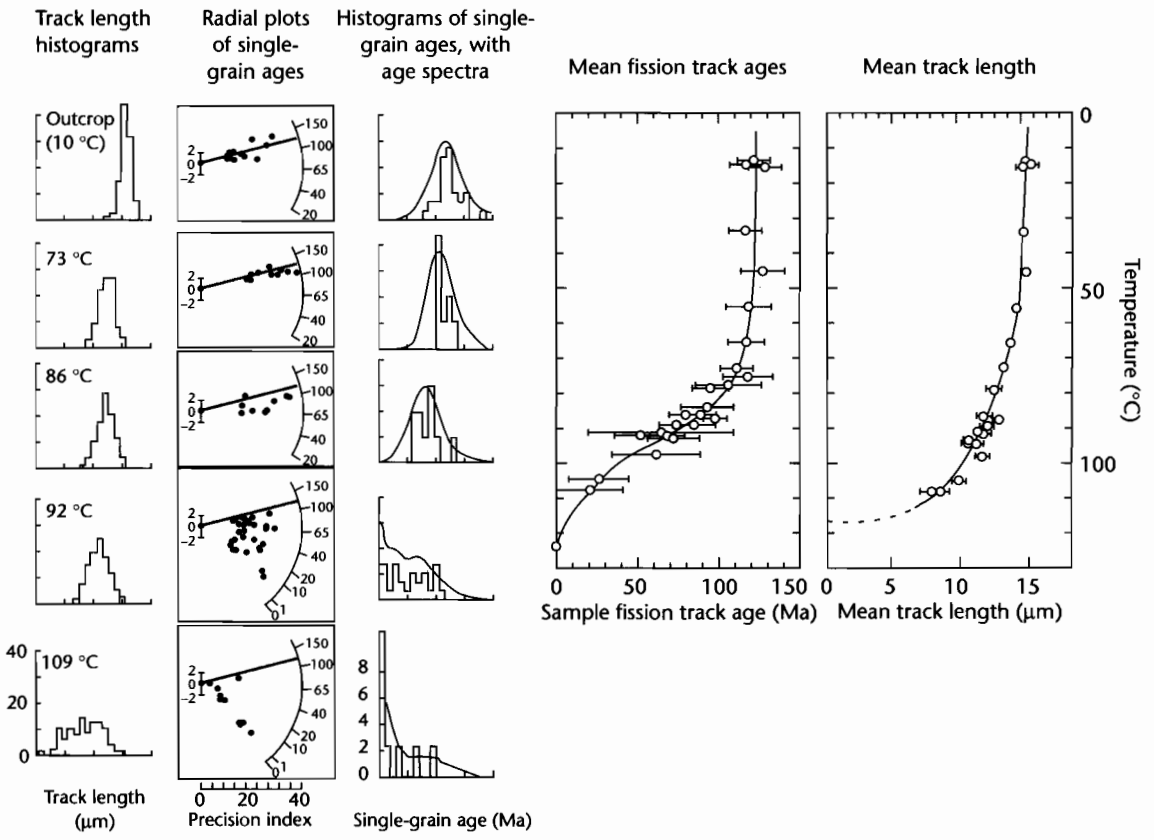

Fig. 9.25 Apatite fission track data from the Otway Basin, southeast Australia (Gleadow and Duddy 1981). The stratigraphic age of the samples is *c.* 120 Ma (shown on the radial plots as a grey band). Note the progressive annealing of fission tracks and reduction of fission track ages of single grains with depth of burial. Reproduced courtesy of Annual Reviews, Palo Alto.

This is because the temperature range over which apatite fission track analysis is sensitive (*c.* 50–120 °C) is also the temperature range over which hydrocarbons are generated (Gleadow et al. 1983). The fission track data from the Otway Basin of Australia (Gleadow and Duddy 1981) illustrate the important principles (Fig. 9.25). At shallow depths above the PAZ, the fission track lengths are tightly clustered and long (*c.* 14 μm), indicating minimal annealing. The fission track age is more or less equivalent to the stratigraphic age of the samples (120 Ma). With greater depth, fission track length histograms show a wider distribution and a shorter mean track length. The fission track ages decrease due to the greater amount of annealing at elevated temperatures, reaching 0 Ma at a temperature of 120 °C (Fig. 9.25).

Apatite fission track analysis of a number of samples at different depths in a sedimentary basin has been used to calculate geothermal gradients. We have seen in §9.6 that there is a number of factors that may affect the distribution of temperature with depth, including variations in thermal conductivity, effects of fluids, and internal heat generation. Consequently, calculation of geothermal gradients from apatite fission track data alone are likely to be significantly in error. Combination of paleothermal data from apatite fission track, vitrinite reflectance, and any other available techniques is therefore always advised.

9.7.4 Thermochronology: U–Th/He method

The accumulation of ^{4}He from the decay of U and Th can also be used as a thermochronological tool (Wolf et al. 1996). The basis for U–Th/He dating is that ^{4}He nuclei (α particles) are produced by the decay of ^{238}U, ^{235}U and ^{232}Th. The helium produced diffuses from the crystal over time, escaping through its surface faces. The rate of diffusion scales on temperature with an Arrhenius-type relationship (eqn 9.40).

$$\frac{\kappa}{a^2} = \frac{\kappa_\infty}{a^2} \exp(-E_a/RT) \tag{9.57}$$

where κ is the diffusivity, κ_∞ is the diffusivity at an infinite temperature, and a is the diffusion domain radius, which may be the physical grain dimension. Diffusivities are measured in the laboratory for certain minerals with different chemical compositions, grain size, and shape. He diffusivity is best understood in apatite. Laboratory data suggest that the closure temperature for the retention of helium is *c.* 80 °C in apatite (Zeitler et al. 1987), so U–Th/He methods extend the temperature range of sensitivity to lower temperatures compared to apatite fission track analysis. This gives additional data on the thermal evolution of the upper 1–2 km of the crust or sedimentary basin-fill.

However, the diffusivity behavior in natural settings is more problematic. One method of investigating this is to study the He age distribution in boreholes where the temperature distribution with depth is known. He ages are predicted to decrease rapidly downhole, because of the effect of temperature on diffusion rates (Wolf et al. 1998). Consequently, there is a Helium Partial Retention Zone (HePRZ), which extends from approximately 40 °C to 80 °C. This is conceptually similar to the Partial Annealing Zone (PAZ) in fission track analysis. The existence of a HePRZ was confirmed by Stöckli et al. (2000) who found a HePRZ overlying an apatite PAZ in samples taken from the White Mountains of California.

Cooling ages from (U–Th)/He diffusion are most simply related to the time of cooling of a sample through its closure temperature. Rapid cooling of samples during exhumation may reveal a fossil or paleo-HePRZ, as we have seen with apatite fission track analysis. Stöckli et al. (2000) recognized a distinct break in slope at 12 Ma when apparent He ages were plotted against depth, signifying the onset of rapid exhumation caused by extensional faulting in the White Mountains of eastern California (Fig. 9.26). This event is barely recognizable from the distribution of apatite fission track apparent ages.

The use of the U–Th/He technique is still in its infancy, and it remains to be discovered where the technique works best and where it suffers from insurmountable problems. In combination with apatite fission track analysis, and thermochronometry using different host minerals such as zircon and titanite, it appears to offer major benefits in evaluating thermal histories within the upper few km of the Earth (Reiners 2002). At present, its application to the thermal history of sedimentary basins is strongly outweighed by its application to exhumation histories.

9.7.5 Mineralogical indices

Mineralogical parameters are controlled by the temperature and chemical properties of the diagenetic environment of the sediment (Fig. 9.27). A number of diagenetic models now exist (e.g., Frey et al. 1980; Burley et al. 1985; Worden and Morad 2003) that allow an interpretation of the sequence of authigenic minerals in terms of their relationship to their depositional environment or surface chemistry (*eogenesis*), the burial or subsurface conditions (*mesogenesis*), and the weathering or re-exposure to surface conditions (*telogenesis*). The reader is referred to §10.4.3 on sandstone reservoirs for further details.

Since eogenetic changes are strongly related to depositional environment, climate, and associated pore-water chemistry, they are of limited use in thermal modeling. However, mesogenesis marks the removal of the sediment from the predominant influence of surface agents in the interstitial pore water. A number of temperature dependent reactions commonly take place in siliciclastic rocks. Kaolinite transforms to dickite, smectites transform to illite via a process of interlayering, and chloritization takes place. Physical processes accompany these chemical changes during burial diagenesis. The most important result is *compaction* due to the weight of the overlying sediments (§9.2). In sandstones, compaction brings about a number of porosity-reducing adjustments including initial mechanical compaction, which simply compresses grains together, rotation, grain slippage, brittle grain deformation and fracturing and plastic deformation of ductile grains.

The best-documented mineral transformations of use in evaluating thermal maturity are from shaly mudstones, where the clay mineral assemblages, the position of the (001) reflection of smectite, the percentage of illite layers in the mixed layer illite 2:1 expandable, and the illite

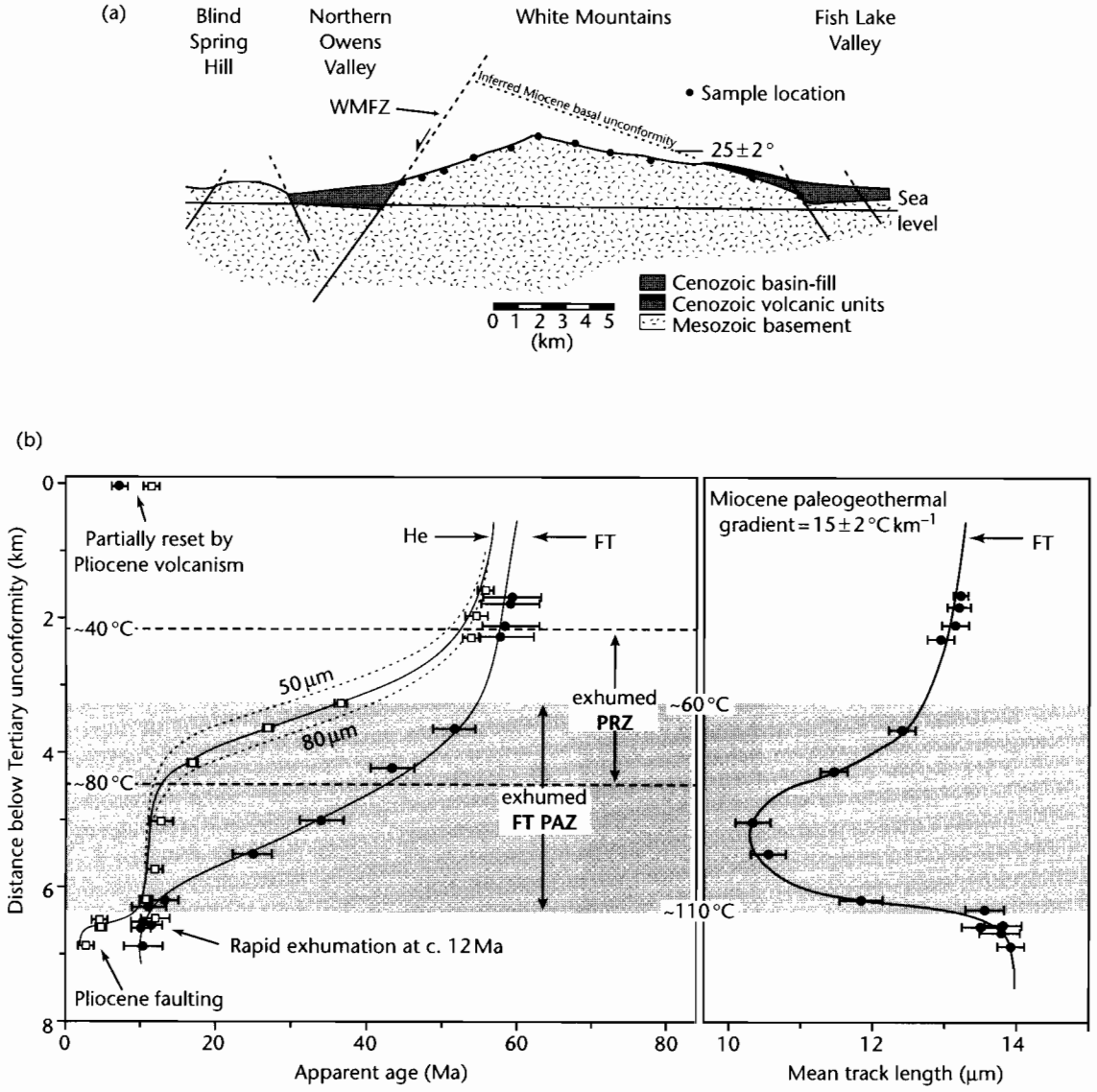

Fig. 9.26 (a) Cross-section of the northern White Mountains, east-central California and west-central Nevada, showing the tilted fault block geometry. The main border fault (White Mountains Fault Zone, WMFZ) has a total of 8–9 km normal displacement, resulting in a 25° eastward tilt recorded by Tertiary volcanic rocks; (b) Integrated apatite fission track and U–Th/He data showing an exhumed partial annealing zone for apatite fission tracks and an exhumed partial retention zone for U–Th/He. Samples from below the exhumed PRZ are invariant with age and directly date the time of inception of footwall cooling caused by extensional faulting. After Stöckli et al. (2000). Reproduced courtesy of Geological Society of America.

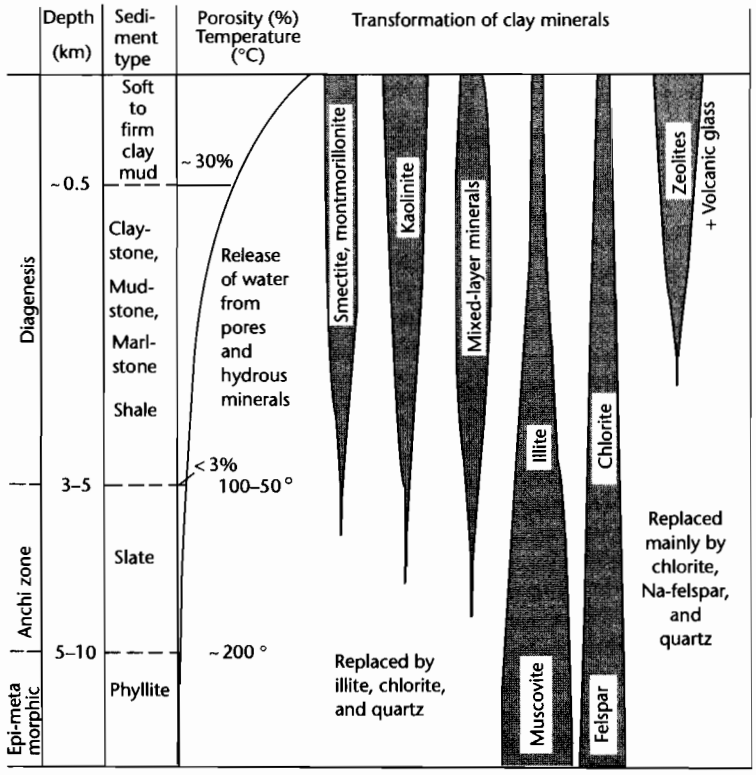

Fig. 9.27 Diagenesis of clay-rich sediments as a function of depth and temperature, showing the most important mineral transformations (after Frey et al. 1980). Reproduced courtesy of Springer.

crystallinity index are used. The approximate relationship between mineralogical changes of this type and organic maturity indices has been attempted (Fig. 9.28). One of the fundamental problems is the need for quantitative indices with which to correlate temperature-driven changes. Kübler et al. (1979) for example, proposed a quantitative measure of the crystallinity of illite using the width of the illite peak on an X-ray diffractogram measured at half of the peak height. The beginning of oil generation ($R_o = 0.5\%$) has been correlated with the disappearance of smectite (e.g., Powell et al. 1978; Kübler et al. 1979).

Quartz cementation and consequent porosity loss is also a temperature-related process acting in sandstones buried to temperatures above 60 °C (Walderhaug 1996). At about the same temperature of 60 °C, smectite clay starts to react with K-felspar to form illite (Hower et al. 1976; Nadeau and Reynolds 1981). At higher temperatures of 100–120 °C, illite precipitates at the expense of kaolinite and K-felspar (Bjorlykke et al. 1986). This can be seen in the percentage of illite in the clay fraction of sandstones penetrated by wells on the Norwegian continental shelf (Fig. 9.29). Quartz cementation and illite precipitation are both temperature dependent, with activation energies of *c.* 15 kcal mol^{-1} and 20 kcal mol^{-1} respectively. The combined temperature-driven effects of quartz cementation and illite precipitation makes sandstones that have experienced temperatures above 120 °C unattractive as potential reservoirs and aquifers (§10.4).

The K content of diagenetic illites allows the age of illite growth to be calculated using the ^{40}K–^{40}Ar radiometric technique. K–Ar ages from samples obtained from different depths can then be used to plot age-depth relationships (Hamilton et al. 1989). The K–Ar age should, for a continuously subsiding basin, increase with depth, since the deeper horizons should reach the critical tem-

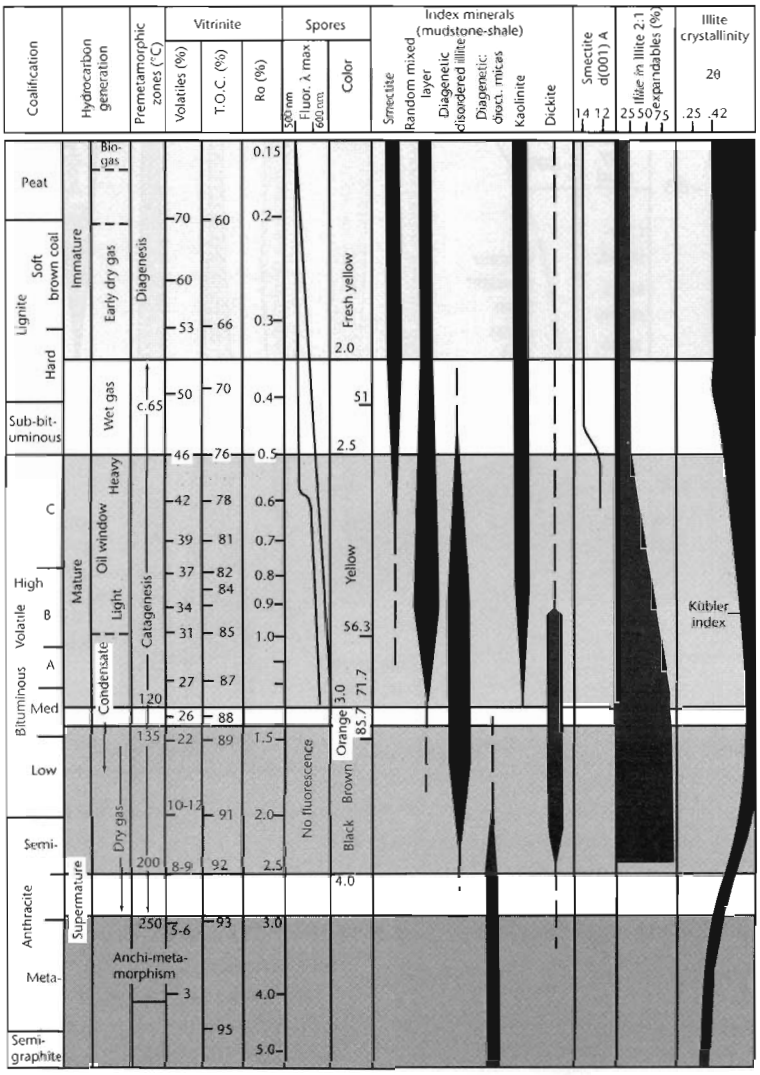

Fig. 9.28 Comparison of a range of thermal indices, modified from Héroux et al. (1979). Thermal indices shown are coal rank, vitrinite total organic carbon and % volatiles, vitrinite reflectance, spore fluorescence and coloration, typical clay mineral distributions, position of the (001) reflection of smectite, % illite in the mixed layer illite 2 : 1 expandable, and illite crystallinity (Kübler index). These indices are correlated with temperature and hydrocarbon products generated.

perature for illite cementation first. A study of sandstone reservoir rocks from the Brent province of the North Sea showed that illite growth began at temperatures of 100–110 °C (corresponding to a vitrinite reflectance in overlying shales of 0.62%), but that there was considerable scatter in the K–Ar age/depth relationship (Hamilton et al. 1992).

9.7.6 Other burial indices

9.7.6.1 Sonic logs

Some indices result from the loss of porosity with increasing burial (§9.2), which is driven by the effective stress on framework grains. Although porosity estimates can be

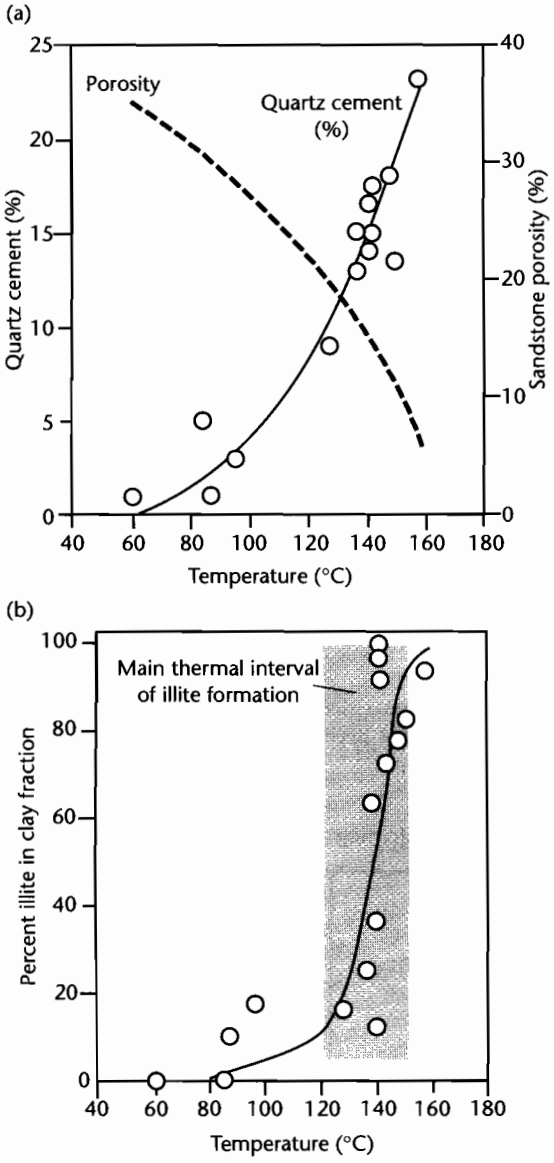

Fig. 9.29 (a) Plot of temperature versus quartz cement content and porosity for wells from the Norwegian continental shelf (Bjorkum and Nadeau 1998), showing an exponential increase in amount of quartz cement with depth; (b) Plot of temperature versus diagenetic illite content measured by X-ray diffraction. Increasing illite content severely reduces permeability. The main thermal interval for illite formation is 120–150 °C.

obtained from a number of downhole logging devices (§9.2.3), the most widely used is the sonic log (Bulat and Stoker 1987; Menpes and Hillis 1995). For a given lithology, such as shales, the curve of sonic interval transit time versus depth reflects the maximum depth (or minimum porosity) attained by a given interval. The curve commonly has an exponential form, so porosity variations at great depth are small.

Two effects are important in the interpretation of sonic log porosity curves. (i) If a sedimentary basin is overpressured, the pore fluid reduces the effective stress on framework grains and impedes compaction. Consequently, overpressured sections have offset porosity–depth curves compared to the "normal" curve. (ii) Uplift and erosion of the basin-fill causes strongly compacted sedimentary rocks to occur at shallower depths. The amount of uplift can be estimated from the offset of the sonic porosity–depth curve of the uplifted section (Fig. 9.30) (Giles and Indrelid 1998; Ware and Turner 2002).

9.8 APPLICATION OF THERMAL MATURITY MEASUREMENTS

9.8.1 Vitrinite reflectance (R_o) profiles

Vitrinite reflectance measurements can be plotted as a function of depth to give R_o profiles. The slope of the R_o curves gives an indication of the geothermal gradients in the history of the basin. Although many profile shapes are possible (Fig. 9.31), they generally indicate an exponential evolution of the organic matter with time (Dow 1977), as expected from the kinetics described in §9.5. In basins largely unaffected by major unconformities, young dip-slip faulting and localized igneous activity, there should therefore be a linear relationship between depth and log R_o. Plots of large numbers of reflectance measurements from many sedimentary basins worldwide (Rowley and White 1998) or from many locations within a basin system (Corcoran and Clayton 2001) show a strong clustering along a roughly linear trend in depth–log R_o space, with an intercept at a depth of zero of 0.2–0.4% (Fig. 9.21).

Individual R_o profiles follow a number of different trends, each of which is diagnostic of a particular thermal history. An example of a simple, sublinear profile is the Terrebonne Parish Well in Louisiana (Heling and Teichmilller 1974) (Fig. 9.32a). R_o is 0.5% at 3 km and 1% at 5 km. It indicates a normal and constant geother-

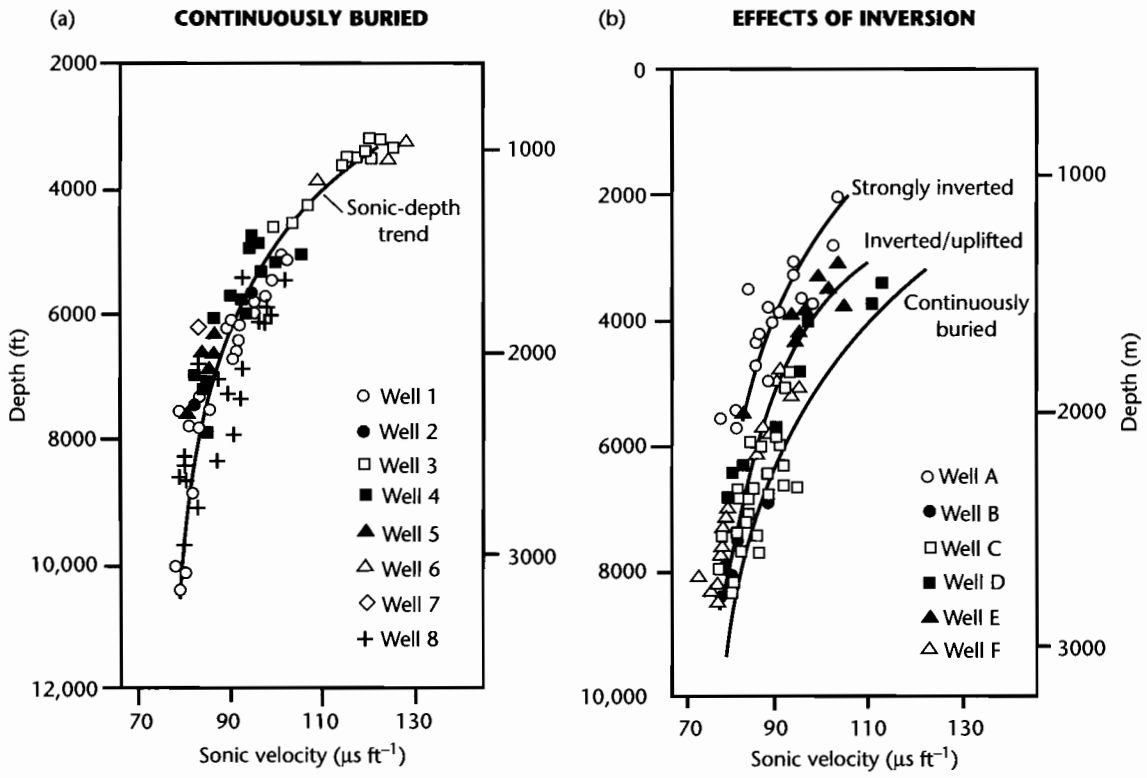

Fig. 9.30 (a) Sonic transit time versus depth for a continuously buried sedimentary succession; (b) Offset of sonic transit time versus depth trends for wells penetrating successions that have been uplifted (after Giles 1997). Reproduced courtesy of Springer.

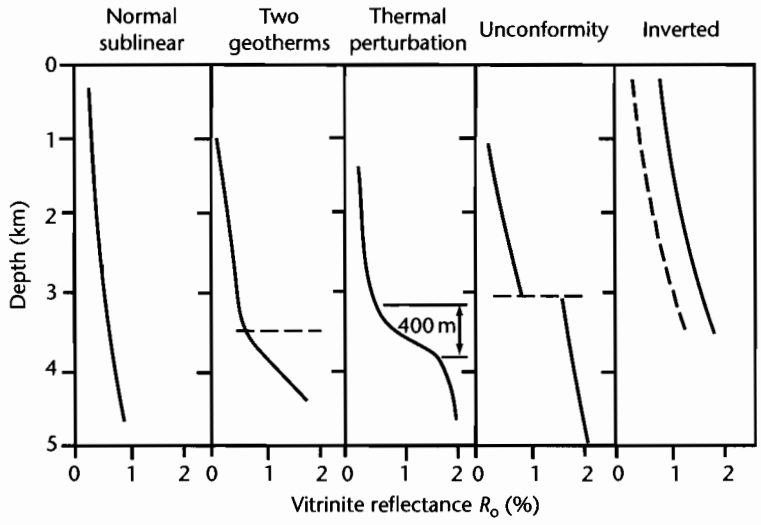

Fig. 9.31 The main types of R_o profile. 1, normal sublinear (constant geothermal gradient); 2, dogleg, two periods with different geothermal gradient; 3, strong thermal perturbation, returning to normal; 4, jump in R_o profile due to unconformity; 5, offset R_o profile in inverted basin.

mal gradient through time. The Woodford Shale of the Anardarko Basin is another example of a sublinear R_o profile with a surface intercept at $R_o = 0.2\%$, indicating the amount of maturation that the vitrinite had undergone prior to deposition (Fig. 9.32b).

Other R_o profiles are more complex. A dogleg pattern of two linear segments of different slope indicates that two periods of different geothermal gradient have occurred. This may result from a thermal "event" occurring at the time presented by the break in slope. Such an interpretation is plausible for the R_o profiles from boreholes in the Rhine Graben (Teichmüller 1970, 1982; Robert 1988) (Fig. 9.33).

R_o profiles may consist of two sublinear segments offset by a sharp break or jump in R_o values. The jump may correspond to an unconformity with a large stratigraphic gap. This is well illustrated in the Mazères 2 borehole in the Lacq area of the Aquitaine Basin, France (Fig. 9.34), where R_o values jump from *c.* 0.8% to *c.* 2.4% at the level of an unconformity separating Aptian–Albian rocks from underlying Kimmeridgian.

If there is a known (logarithmic) relationship of R_o with depth and the subsidence history of a sedimentary basin is known, the R_o values give an indication of the variation of the geothermal gradient through time. This then allows different tectonic histories to be tested (Middleton 1982).

9.8.2 Estimation of denudation from R_o profiles

R_o profiles can be used to estimate the amount of denudation resulting from a period of basin inversion, since the vitrinite locks in information about the maximum paleotemperature experienced. The technique has been used extensively, particularly in the region of the British Isles where an important crustal uplift event took place in the Early Tertiary (Rowley and White 1998). This uplift event, which was most likely related to the thermal, isostatic, and dynamic effects of the Icelandic plume (White 1988; Brodie and White 1994), caused an unconformity that cuts down variably into Mesozoic rocks. The paleotemperature profiles from areas such as the Irish Sea Basin system are linear and subparallel to the present-day geotherm (Duncan et al. 1998), suggesting that heating was caused primarily by burial rather than by basal heat flow variations or local magmatic and fluid flow effects. However, most of the R_o values in boreholes in the British–Irish area have elevated

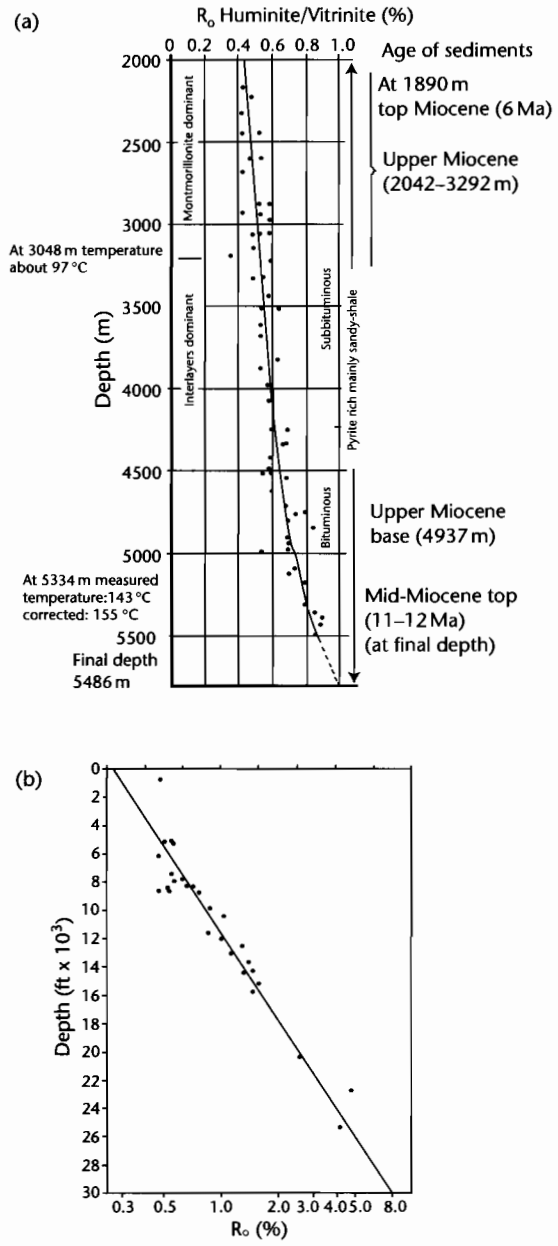

Fig. 9.32 (a) Vitrinite reflectance profile for Terrebonne Parish, Pont au Fer well in Louisiana. The profile is sublinear and continuous, suggesting a near-constant geothermal gradient through time (after Heling and Teichmüller 1974); (b) Woodford Shale of the Anadarko Basin also shows a good sublinear trend (Cardott and Lambert 1985). Note logarithmic scale.

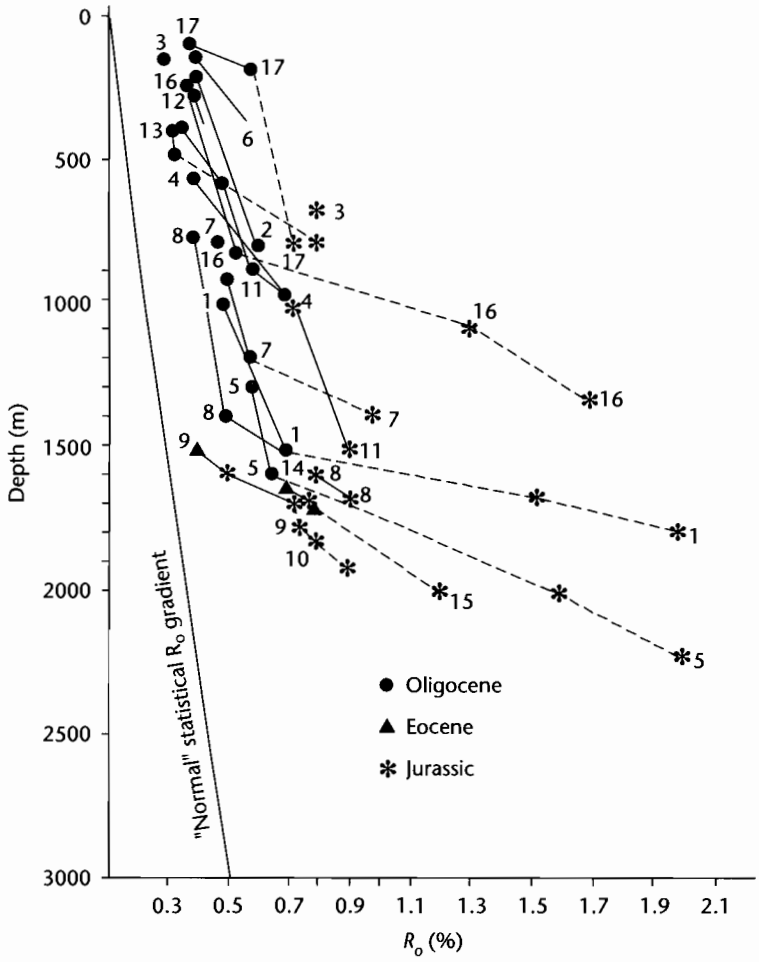

Fig. 9.33 Reflectance profiles from a number of wells in the Alsace region of the Rhine Graben (after Teichmüller 1970). In general, there are pronounced doglegs in the R_o profiles at about the age of the Oligocene–Eocene boundary. The post-Eocene history shows a "normal" gradient, whereas the pre-Oligocene sedimentary rocks have high reflectance values in relation to their depth of burial. This suggests that rifting in the late Eocene caused higher than normal maturity in the older rocks of the basin-fill.

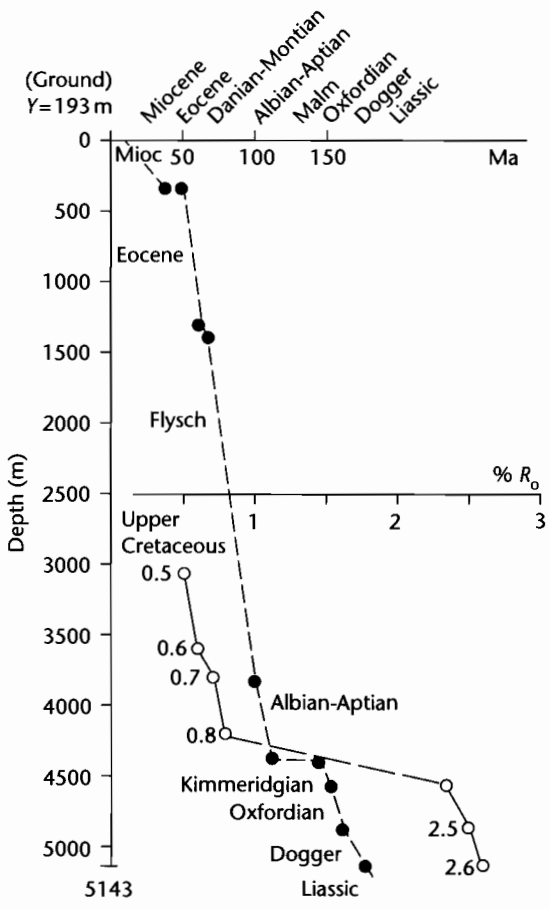

Fig. 9.34 Stratigraphic depth and vitrinite reflectance profiles for the Mazères 2 borehole in the Lacq region of southern France. The sharp increase in R_o marks an unconformity between the Lower Cretaceous and the Upper Jurassic (after Robert 1988).

values compared to the global dataset of noninverted basins (Fig. 9.35) (Corcoran and Clayton 2001). Calculations of the amount of denudation from the R_o profile can be performed using a number of different methods:

1 The curve of log R_o versus depth is extrapolated linearly upwards to a value of approximately 0.2% R_o (Dow 1977; Corcoran and Clayton 2001). The displacement of the depth axis is the amount of denudation. Although this method has been very widely applied, it makes the erroneous assumption that the geothermal gradient is linear. This is a particularly poor assumption in the shallow parts of basins where thermal conductivities vary strongly. It is more likely that the geotherm is convex near the surface (Figs. 9.14, 9.15). Secondly, large errors may result from the incorrect choice of surface temperature (and therefore R_o at $y = 0$) at the time of maximum paleotemperatures.

2 Maximum depths of burial can be estimated from VR values from empirical relations such as (Barker and Pawlewicz 1986)

$$\ln R_0 = 0.0096T - 1.4 \tag{9.58}$$

where T is the temperature, which must be converted to depth using a geothermal gradient. The empirically derived depth can be compared with the present-day depth of the sample. However, there are large uncertainties in the accuracy of the R_o–T relationship, and geotherms may be unknown.

3 Vitrinite reflectance can be calculated from a forward thermal model using the kinetic approaches described in §9.5 (e.g., Middleton 1982). A comparison of observed VR values with the results of a number of forward models allows the most likely parameter values and amount of denudation to be estimated. Alternatively, the amount of denudation can be estimated by inverse methods using the same chemical kinetics.

Increasingly, vitrinite reflectance data are interpreted alongside other thermal indicators, such as apatite fission track thermochronometry. Both techniques require a conversion to temperature. It is estimated that total fission track annealing in apatites (closure temperature) with typical Cl content corresponds to a vitrinite reflectance value of 0.7%. This in turn corresponds to a temperature of 110–120 °C.

9.9 GEOTHERMAL AND PALEOGEOTHERMAL SIGNATURES OF BASIN TYPES

We have previously seen that vitrinite reflectance measurements and apatite fission track and (U–Th)/He analysis can be used to constrain paleotemperatures and paleogeothermal gradients. This then helps to determine the formative mechanism of the basin. Robert

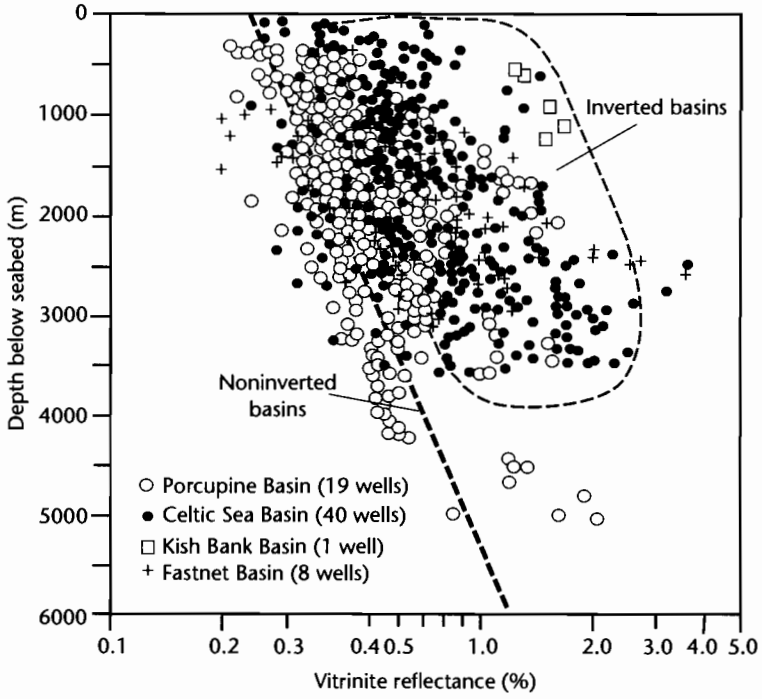

Fig. 9.35 Vitrinite reflectance versus depth for Mesozoic and Cenozoic successions penetrated in boreholes in a number of basins offshore Ireland (Corcoran and Clayton 2001). Basins such as the Porcupine Basin show a "normal" R_o profile indicative of continual subsidence, whereas those basins that have experienced tectonic uplift and exhumation (such as the Celtic Sea, Kish Bank, and Fastnet Basins) have displaced R_o profiles indicating higher thermal maturity than expected from the present depth of burial.

(1988) suggested three main types of paleogeothermal history: (i) basins with normal or near-normal paleogeothermal history, (ii) cooler than normal basins, and (iii) hotter than normal basins.

(i) Basins with normal or near-normal paleogeothermal history

Old passive margins have present-day geothermal gradients of *c.* 25–30 °C km^{-1} (Congo 27 °C km^{-1}, Gabon 25 °C km^{-1}, Gulf Coast USA 25 °C km^{-1}). The Terrebonne Parish Well (Fig. 9.32a) shows a vitrinite reflectance of about 0.5% at a depth of 3 km and the shape of the curve is sublinear. Mature passive margins therefore have near-normal geothermal gradients.

(ii) Cooler than normal (*hypothermal*) basins

Hypothermal basins include oceanic trenches, outer forearc and foreland basins. Ocean trenches are cold, with surface heat flows often less than 1 HFU (42 mW m^{-2}). In the Japanese archipelago Eocene–Miocene coals occur in two regions: one in Hokkaido in the north along a branch of the present-day Japan trench, and the other in Kyushu in the south is situated in a volcanic arc position relative to the Ryu-Kyu trench (Fig. 9.36). Figure 9.37 shows the R_o profiles for the two different regions. The Hokkaido region is cold with poorly evolved coals (sub-bituminous coals with R_o = 0.5% still occurring at a depth of 5 km) whereas the volcanic arc in Kyushu is hot, containing anthracites (>2% R_o). The Mariana Trench, which is a southward continuation of the Japan Trench, and its forearc region are also cold, with surface heat flows of less than 1 HFU (42 mW m^{-2}).

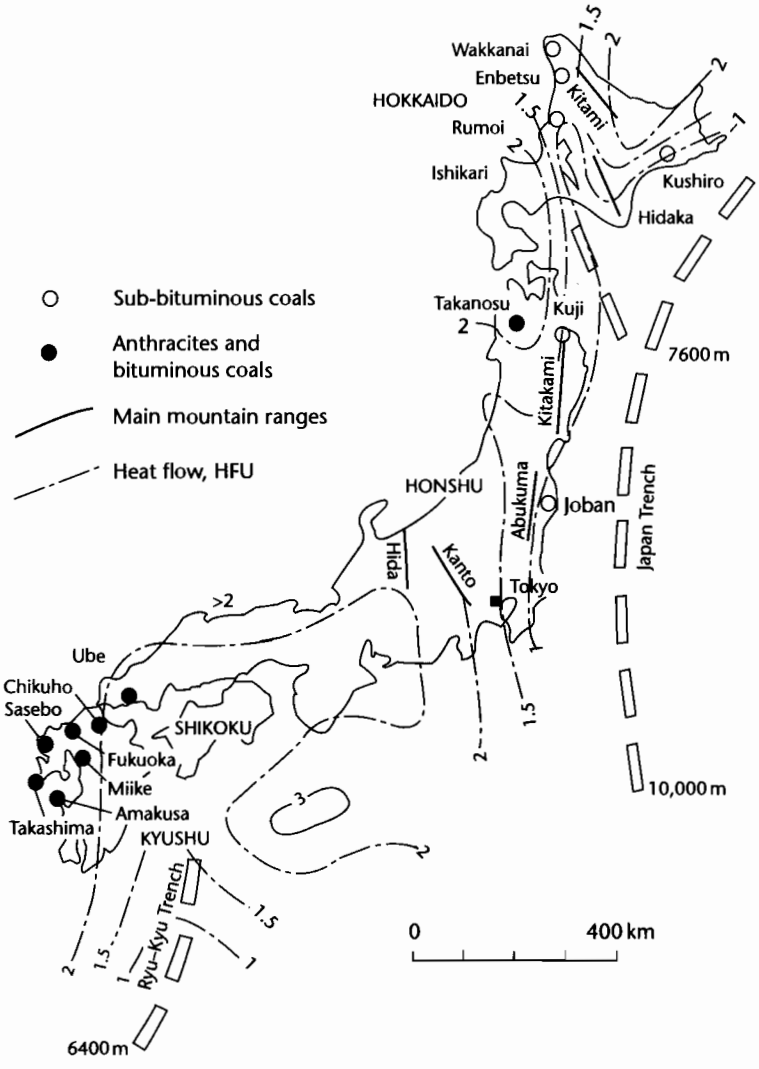

Fig. 9.36 The deposits of Tertiary coals in Japan and the surface heat flows in HFU (Aihara 1980). Note that anthracites and bituminous coals are found in Kyushu and the extreme southwest of Honshu, whereas sub-bituminous coals are found in the north of Honshu and on Hokkaido.

Foreland basins are also characterized by low present-day geothermal gradients, 22 °C km^{-1} to 24 °C km^{-1} being typical of the North Alpine Foreland Basin in southern Germany (Teichmüller and Teichmüller 1975; Jacob and Kuckelhorn 1977). The Anzing 3 well near Munich penetrates the autochthonous Molasse, undisturbed by Alpine tectonic events. At the base of the Tertiary at 2630 m depth the R_o is still only 0.51%. The Miesbach 1 well cuts through about 2 km of thrust sheets of the frontal thrust zone of the Alps (the subalpine zone), before penetrating the autochthonous sediments to a depth of 5738 m (Fig. 9.38). Even at this great depth, the R_o is still only 0.6%, indicating an abnormally low geothermal gradient during the Tertiary. The greater subsidence rate at Miesbach 1 (nearly 0.3 mm yr^{-1}) compared with Anzing 1 (0.1 mm yr^{-1}) may have been responsible

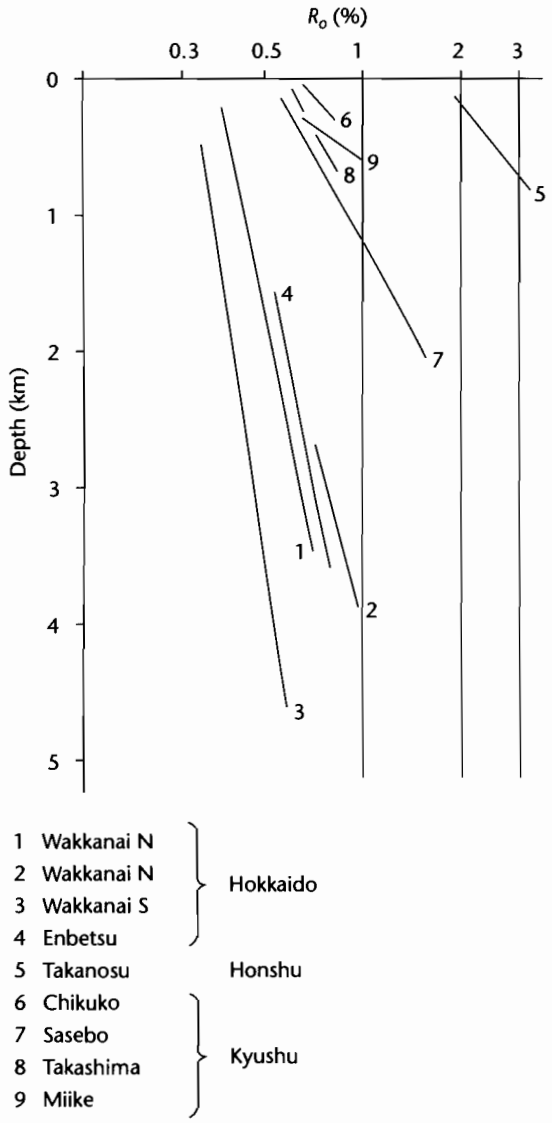

Fig. 9.37 Vitrinite reflectance profiles for the locations shown in Fig. 9.36. The first set of locations (1–4) belong to a branch of the oceanic Japan trench system running along the east of Japan; they are characterized by low reflectances and are associated with low present-day heat flows. The second group of locations (6–9) corresponds to the internal arc relative to the Ryu-Kyu trench. These locations are highly evolved at shallow depths of burial and are associated with high present-day heat flows. The single location 5 from the NW of Honshu occurs in the present volcanic arc area where the heat flows exceed 2 HFU, and the vitrinite reflectance is very high. There is thus a clear relationship between tectonic environment and geothermy. After Robert (1988).

for the very low geothermal gradient in the former. The low present-day geothermal gradients (Anzing 3, 22.8 °C km^{-1}, Miesbach 1, 23.5 °C km^{-1}) may have been even lower in the past during the phase of rapid subsidence related to continental collision and flexure.

(iii) Hotter than normal (*hyperthermal*) basins

Hyperthermal basins are found in regions of lithospheric extension such as backarc basins, oceanic and continental rift systems, some strike–slip basins, and the internal arcs of zones of B-type subduction. This follows from the mechanics of basin formation in stretched regions, involving the raising towards the surface of isotherms.

Oceanic rifts are zones of very high heat flows, 3–4 HFU (120–170 mW m^{-2}) being typical and values occasionally reaching 5–6 HFU (200–250 mW m^{-2}). Some Californian *strike–slip basins* have very high geothermal gradients (*c.* 200 °C km^{-1} in Imperial Valley), so that very young sediments can be highly mature. Continental rifts have high present-day geothermal gradients (>50 °C km^{-1} in the Red Sea, up to 100 °C km^{-1} in the Upper Rhine Valley) and ancient continental rifts have high organic maturities in their basin sediments.

Oceanic measurements and deep boreholes in the *Red Sea* (Girdler 1970) suggest that high surface heat flows (generally >3 HFU, >125 mW m^{-2}) occur in a broad band at least 300 km wide centered on the axis of the rift. The organic maturation shown by R_o profiles and the occurrence of oil, gas, and condensate fields suggests that the highest maturity is found in the south of the Red Sea, intermediate values are found in the north of the Red Sea, and the lowest occur in the Gulf of Suez. This can be correlated with different amounts of extension, the largest amount being in the south of the Suez–Red Sea system. The former elevated heat flows in the Oligo–Miocene of the Gulf of Suez have now diminished to near-normal values, while the southern Red Sea, which is still actively rifting, still has very high heat flows.

There are many other examples of high organic maturation in ancient continental rift basins: 2–3% R_o in the Lower Cretaceous of the Congo; 3.3% R_o in the Upper Cretaceous of Cameroon; 3.5% R_o in the Coniacian of the Benue Trough, Nigeria; 5% R_o in the Permian of the Cooper Basin, Australia.

Internal arc heat flows are elevated because of magmatic activity. The Tertiary anthracites of Honshu, Japan (see

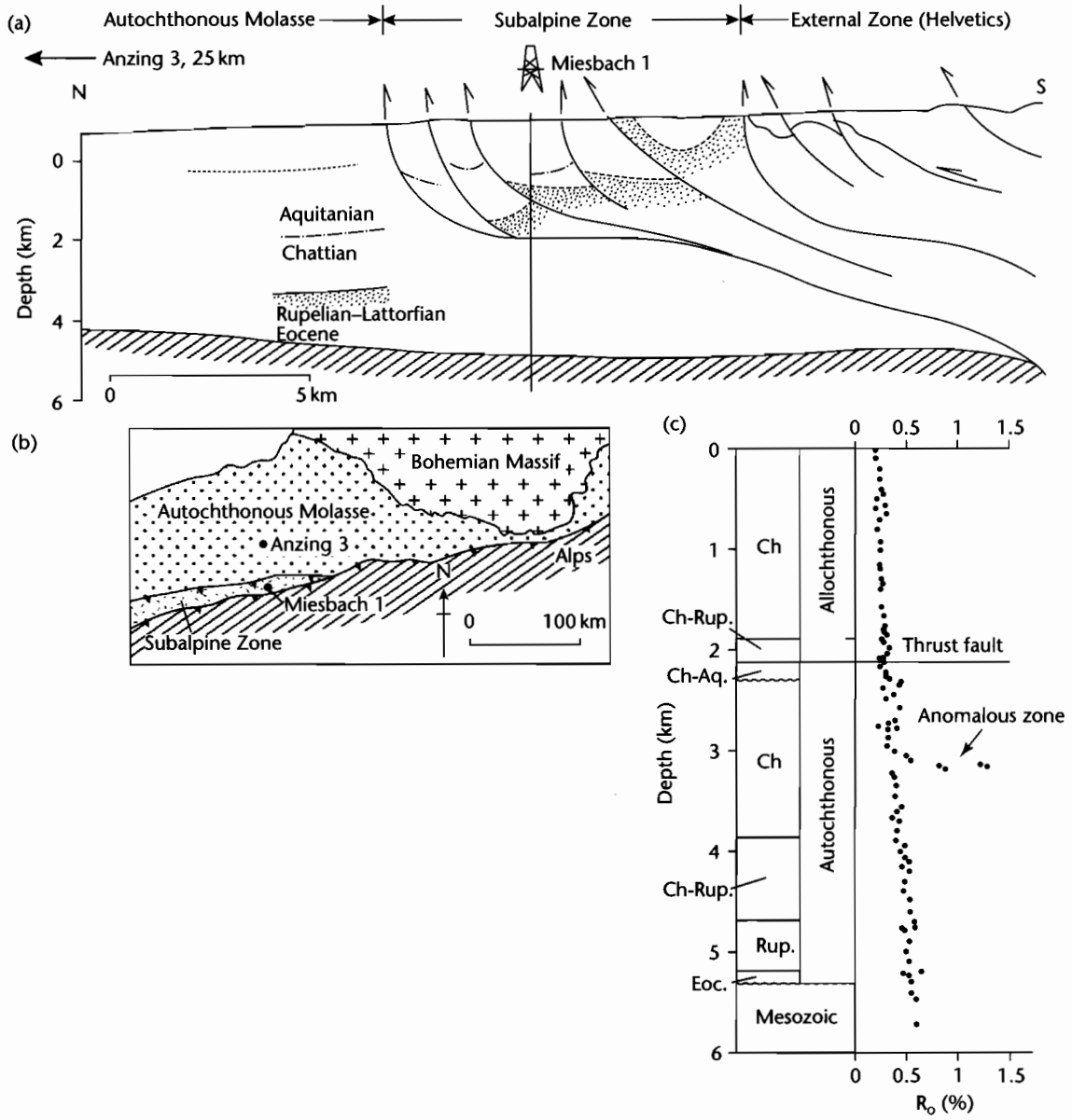

Fig. 9.38 (a) Location of the Bavarian part of the North Alpine foreland basin in southern Germany. Anzing 3, near Munich, and Miesbach 1, are boreholes discussed in the text; (b) Cross-section of the southernmost part of the Bavarian section of the North Alpine foreland basin, showing the location of Miesbach 1 in the tectonically imbricated subalpine zone (after Teichmüller and Teichmülller 1975); (c) The R_o profile at Miesbach 1 (Jacob and Kuckelhorn 1977) shows that the autochthonous "Molasse" under the basal subalpine thrust is poorly evolved, not exceeding 0.6% even at 5738 m depth. This is indicative of a very low geothermal gradient during the period of rapid sedimentation in the Oligocene.

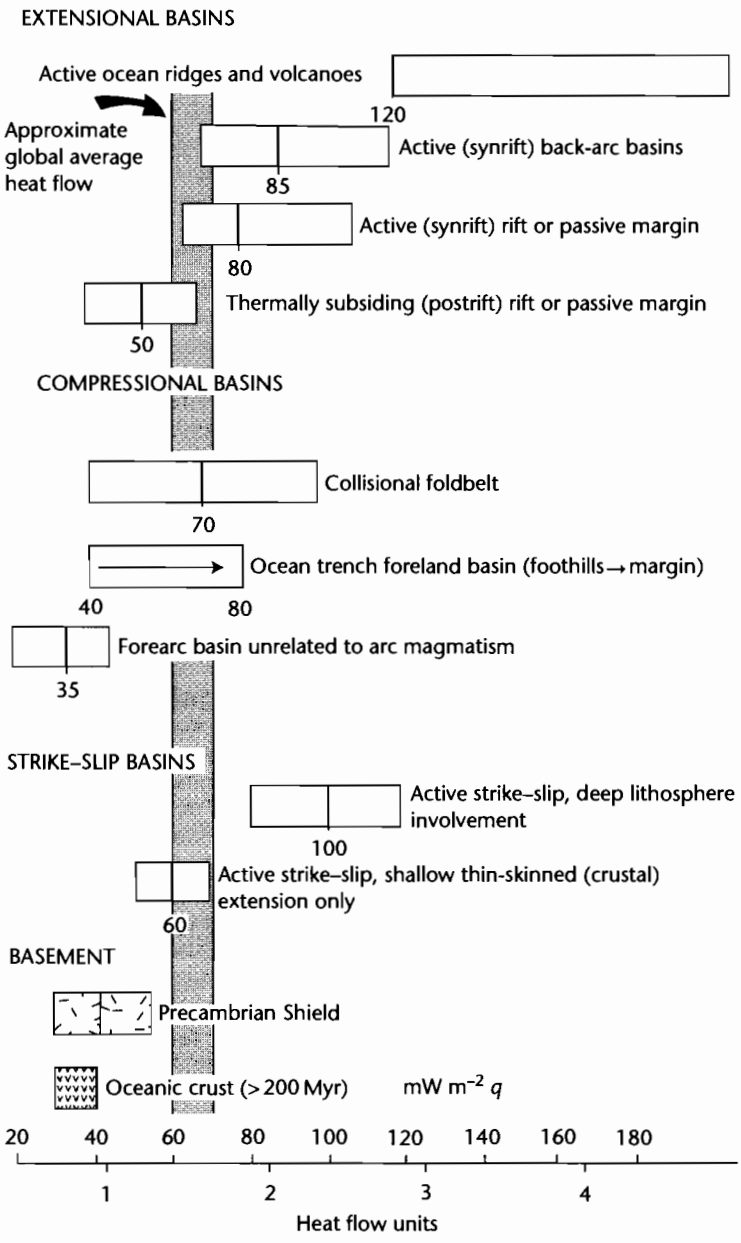

Fig. 9.39 Summary of the typical heat flows associated with sedimentary basins of various types.

above) (2–3% R_o) are an example. Similar patterns are found in ocean–continental collision zones such as the Andean Cordillera, and hyperthermal events may also affect parts of continent–continent collision zones such as the Alps: the "Black Earths" of southeastern France have R_o values of over 4%, but the precise origin of the thermal event is unknown (Robert 1988, p. 261).

The heat flows of the main genetic classes of sedimentary basin are summarized in Figure 9.39.